Understanding ice supersaturation, particle growth, and number concentration in cirrus clouds

Jennifer M. Comstock,[1] Ruei-Fong Lin,[2,3] David O'C. Starr,[3] and Ping Yang[4]

Received 28 April 2008; revised 9 September 2008; accepted 19 September 2008; published 10 December 2008.

[1] Many factors control the ice supersaturation and microphysical properties in cirrus clouds. We explore the effects of dynamic forcing, ice nucleation mechanisms, and ice crystal growth rate on the evolution and distribution of water vapor and cloud properties in nighttime cirrus clouds using a one-dimensional cloud model with bin microphysics and remote sensing measurements obtained at the Department of Energy's Atmospheric Radiation Measurement (ARM) Climate Research Facility located near Lamont, OK. We forced the model using both large-scale vertical ascent and, for the first time, mean mesoscale velocity derived from radar Doppler velocity measurements. Both heterogeneous and homogeneous nucleation processes are explored, where a classical theory heterogeneous scheme is compared with empirical representations. We evaluated model simulations by examining both bulk cloud properties and distributions of measured radar reflectivity, lidar extinction, and water vapor profiles, as well as retrieved cloud microphysical properties. Our results suggest that mesoscale variability is the primary mechanism needed to reproduce observed quantities. Model sensitivity to the ice growth rate is also investigated. The most realistic simulations as compared with observations are forced using mesoscale waves, include fast ice crystal growth, and initiate ice by either homogeneous or heterogeneous nucleation. Simulated ice crystal number concentrations (tens to hundreds particles per liter) are typically two orders of magnitude smaller than previously published results based on aircraft measurements in cirrus clouds, although higher concentrations are possible in isolated pockets within the nucleation zone.

Citation: Comstock, J. M., R.-F. Lin, D. O'C. Starr, and P. Yang (2008), Understanding ice supersaturation, particle growth, and number concentration in cirrus clouds, *J. Geophys. Res.*, *113*, D23211, doi:10.1029/2008JD010332.

1. Introduction

[2] The interaction between ice clouds and water vapor in the upper troposphere is critical for properly simulating current and future climates. Cirrus clouds may regulate upper tropospheric humidity and likely play a role in dehydration and transport of water vapor into the stratosphere [*Corti et al.*, 2006; *Immler et al.*, 2007]. Ice supersaturated regions are prevalent both in and outside cirrus clouds [*Jensen et al.*, 2001; *Spichtinger et al.*, 2004; *Comstock et al.*, 2004; *Gettelman et al.*, 2006]. Ice supersaturation is required for ice formation in cirrus clouds, yet most global models do not allow ice supersaturation. A recent study shows that incorporating ice supersaturation into a global model tends to decrease the occurrence of thick cirrus and anvils, and increase stratospheric water vapor [*Gettelman and Kinnison*, 2007]. Only the most recently developed ice nucleation parameterizations for global models require ice supersaturation [*Kärcher and Lohmann*, 2002, 2003; *Liu and Penner*, 2005; *Tompkins et al.*, 2007] and have been demonstrated in global simulations [*Lohmann et al.*, 2004; *Liu et al.*, 2007].

[3] The mechanisms that control ice supersaturation in cirrus clouds are not well understood. One mechanism that could explain large supersaturation (>130%) in cold clouds (colder than $-70°C$) involves the presence of nitric acid on the surface of ice crystals, which could inhibit the uptake of water vapor by the ice [*Gao et al.*, 2004]. Another possible mechanism is the formation of cubic ice, which occurs at temperatures colder than $\sim-80°C$, grows to very small particle sizes, and subsequently increases the water vapor pressure in cold clouds [*Murphy*, 2003; *Murray et al.*, 2005; *Shilling et al.*, 2006]. However, these mechanisms will only contribute to a small fraction of midlatitude cirrus clouds that occur at such cold temperatures.

[4] Ice nucleation mechanism also influences the relative humidity with respect to ice (RHI) in cirrus. Cirrus clouds that form via homogeneous nucleation will have a much higher threshold RHI than those that form via heterogeneous nucleation on insoluble ice nuclei [i.e., *Haag et al.*, 2003; *Koop et al.*, 2000]. It is generally assumed that homogeneous nucleation is the primary mechanism for ice

[1]Atmospheric Science and Global Change Division, Pacific Northwest National Laboratory, Richland, Washington, USA.
[2]Goddard Earth Sciences and Technology Center, University of Maryland, Baltimore County, Baltimore, Maryland, USA.
[3]Laboratory for Atmospheres, NASA Goddard Space Flight Center, Greenbelt, Maryland, USA.
[4]Department of Atmospheric Sciences, Texas A&M University, College Station, Texas, USA.

Copyright 2008 by the American Geophysical Union.
0148-0227/08/2008JD010332

formation in the upper troposphere. While heterogeneous nucleation is the primary ice formation mechanism in warmer mixed phase clouds, its role in upper tropospheric cloud formation is still uncertain. There is some evidence that heterogeneous nucleation can contribute to ice formation in upper tropospheric clouds, particularly at smaller ice supersaturation and weaker updraft velocities than are typical for homogeneous nucleation [*Sassen and Dodd*, 1988]. Parcel model simulations have shown that clouds formed by heterogeneous nucleation may have smaller ice number concentrations (N_i) than ice formed by homogeneous nucleation [*DeMott et al.*, 1997; *Jensen and Toon*, 1997; *Sassen and Benson*, 2000; *Lin et al.*, 2002], and thus a different radiative feedback. Since homogeneous nucleation does not occur at temperatures warmer than approximately $-38°C$, heterogeneous nucleation is certainly the primary ice nucleation mechanism for the warmer temperature range. The ice supersaturation observed in cloudy and clear regions at $T > -38°C$ [*Comstock et al.*, 2004] further indicates the existence of favorable conditions for heterogeneous nucleation to occur provided that sufficient ice nuclei exist. Although a few recent studies have examined the competition between heterogeneous and homogeneous nucleation for temperature below $-38°C$ [*Kärcher et al.*, 2007; *Spichtinger and Gierens*, 2008], the relative importance of these mechanisms at colder temperatures is still uncertain.

[5] The number of nucleated ice crystals in cirrus is determined by the number of solution droplets (e.g., sulfuric acid), ice nuclei (e.g., mineral dust, sulfates, and organics) or pure water droplets that become activated via heterogeneous or homogeneous nucleation. The subsequent evolution of the particle size distribution (PSD) is controlled by the amount of available water vapor and their growth rate. Ice crystals grow by diffusional growth, which is the deposition of water vapor molecules onto the ice crystal, and is closely linked to the ice saturation ratio. However, the physical processes responsible for the construction of the ice lattice at the molecular level remain uncertain. The growth efficiency of ice particles in cirrus models is controlled by the deposition coefficient (α_D; or mass accommodation coefficient), which represents the fraction of water molecules that come in contact with the ice crystal surface and are integrated into the crystal lattice. Although the appropriate value of α_D is somewhat uncertain, recent laboratory studies at low supersaturations (<20%) suggest that α_D can be quite small ($\alpha_D \sim 0.006$), particularly for small ice crystals in the nucleation region of ice clouds [*Magee et al.*, 2006]. In parcel model simulations, the value of α_D can have a significant impact on the number concentration of ice crystals nucleated. *Lin et al.* [2002] demonstrate that the number of nucleated ice particles increases with decreasing α_D. Subsequent model simulations suggest that small α_D produces large ice crystal concentrations that could account for discrepancies between measurements and model simulations of ice crystal number concentrations in cirrus clouds [*Gierens et al.*, 2003] and that α_D may vary with particle size and supersaturation [*Kay and Wood*, 2008].

[6] The dynamic structure of cirrus also influences the RHI and PSDs in cirrus clouds [*Sassen et al.*, 1990; *Gultepe and Starr*, 1995; *Kärcher and Ström*, 2003; *Jensen et al.*, 2005]. The number of particles formed by various nucleation processes is rather sensitive to the strength of the updraft speed [*Lin et al.*, 2002]. While small-scale turbulence is important in the evolution of cirrus [*Gu and Liou*, 2000], intermediate-scale waves likely play a role in cloud development [*Gultepe and Starr*, 1995] and in controlling cirrus properties [*Kärcher and Ström*, 2003]. Updrafts create pockets of ice supersaturated air and initiate ice formation. Representing these cloud-scale processes in large-scale models remains one of the key uncertainties in accurately predicting the feedback of cirrus and upper tropospheric water vapor in global models.

[7] In response to these difficulties in understanding the connection between the RHI and cirrus microphysical properties, we use a combination of measurements from the Department of Energy (DOE) Atmospheric Radiation Measurement (ARM) program [*Ackerman and Stokes*, 2003] and a detailed cloud model to better understand the physical processes that influence the RHI and microphysical properties in cirrus clouds. The primary science question we investigate is what processes influence the frequency distribution of RHI and microphysical properties observed in cirrus clouds? Our approach is to use a cloud model with binned microphysics to understand the processes that control the RHI and produce ice crystal number concentration and microphysical properties consistent with ground based and airborne observations. As part of this analysis, we will evaluate the effects of particle growth rate, nucleation mechanism, and mesoscale variability on the simulated cloud and thermodynamic properties. The structure of this paper is to present (1) the observations and cloud property retrieval algorithms used for model evaluation and initialization, (2) model description, (3) model simulations and comparisons with observations, and (4) discussion and summary.

2. Observations

2.1. Raman Lidar (RL)

[8] The DOE ARM program operates a turn-key, fully autonomous Raman lidar (RL) for profiling water vapor, aerosols and clouds [*Goldsmith et al.*, 1998] at the Southern Great Plains (SGP) ARM Climate Research Facility (ACRF) located near Lamont, OK (36°37′N, 97°30′W). The ARM RL has been used extensively to study the variability of aerosols [*Turner et al.*, 2001], water vapor [*Turner and Goldsmith*, 1999; *Ferrare et al.*, 2004], and clouds [*Comstock et al.*, 2004] in the atmosphere. The ARM RL transmits a laser pulse at 355 nm using a Nd:YAG laser and detects Raman-shifted photons at 387 nm and 408 nm due to the rotational-vibrational Raman scattering off nitrogen and water vapor molecules, respectively. The RL also detects the co-polarized and cross-polarized returns at 355 nm, which is used to compute the depolarization ratio and is useful for distinguishing the ice and liquid phases in optically thin clouds. Because of an increase in solar background energy during daytime, water vapor profiles in the upper troposphere are limited to nighttime observations when profiles can extend to 12 km in cloud free conditions for the configuration of this Raman system. In order to produce profiles with adequate signal-to-noise ratio, the lidar profiles are averaged 10 minutes temporally and between 78 and 400 m vertically depending on altitude (~200 m at 8 km and ~300 m at 10 km).

[9] Using the nitrogen signal and our knowledge of the nitrogen molecular number density (n_{387}) in the atmosphere, we can compute the particle extinction coefficient at 355 nm [*Ansmann et al.*, 1992]:

$$\alpha_{ext}(z) = \frac{\frac{d}{dz}\left[\ln \frac{n_{387}(z)}{S_{387}(z)z^2}\right] - \alpha_{355}^{mol}(z) - \alpha_{387}^{mol}(z)}{1 + \left(\frac{\lambda_{355}}{\lambda_{387}}\right)^k} \quad (1)$$

where S_{387} is the lidar signal received at 387 nm, α_{355}^{mol} and α_{387}^{mol} are the extinction coefficients due to molecular absorption and Rayleigh scattering at their respective wavelengths (λ_{355} = 355 nm and λ_{387} = 387 nm), z denotes the altitude, and k is a factor between 0 and 1 depending on the composition of the scatterers. In this study we use profiles of α_{ext} for model validation and to retrieve cirrus microphysical properties.

[10] Analogously, the water vapor mixing ratio (q_v) is computed at each vertical level using:

$$q_v(z) = C_L \frac{S_{408}(z)}{S_{387}(z)} \quad (2)$$

where C_L encompasses the system calibrations, and S_{408} and S_{387} denote the received lidar signals due to water vapor and nitrogen, respectively. The lidar signal can be described by the lidar equation $S_j(z) = k_{lid\ j}\, z^{-2}\, O_j(z)\sigma_j\, n_j(z) q(\lambda_o, z) q(\lambda_j, z)$ where j denotes the detection wavelength (387 or 408 nm), k_{lid} contains the laser pulse energy, receiver area, and sensitivity of the channel, $O(z)$ denotes the overlap function, σ is the Raman cross section for the specific molecular species (i.e., H_2O, N_2 etc.), $n_j(z)$ is the number density of the molecular species detected at wavelength j, $q(\lambda_o, z)$ is the transmission of the outgoing laser beam, and $q(\lambda_j, z)$ is the transmission of the backscattered signal (see *Turner and Goldsmith* [1999] for further details). These lidar signals include system-dependent corrections such as overlap. Detailed descriptions of computing q_v using the Raman technique and ARM RL calibrations are discussed thoroughly by *Whiteman et al.* [1992] and *Turner and Goldsmith* [1999]. The random error in the water vapor measurement increases with altitude and is on average ~7% at 8 km and ~15 % at 9 km. We do not include any water vapor measurements with random error >20 % in our analysis. We use the RL q_v profiles to initialize the cirrus model and RHI for comparisons with model simulations. RHI is computed using the formula of *Goff and Gratch* [1946] for saturation vapor pressure and temperature profiles are interpolated between 6-hourly radiosondes.

2.2. Millimeter Cloud Radar (MMCR)

[11] Also located at the SGP ACRF facility is a 35 GHz Millimeter Wave Cloud Radar (MMCR) [*Moran et al.*, 1998], which operates autonomously on a continuous basis since November 1996. The SGP MMCR has an antenna diameter of 3 m and a beam width of 0.19°. The MMCR's original configuration provided measurements of reflectivity (Z_e), Doppler velocity (V_D), and spectral width. More recently, the MMCR has been upgraded to record the full Doppler spectra. The overall uncertainty of the reflectivity, Doppler velocity and spectral width are 0.5 dBZ, 0.1 m s^{-1}, and 0.1 m s^{-1} [*Widener and Johnson*, 2005], respectively. Specific instrument details for both the ARM RL and MMCR can be found at http://www.arm.gov. We use the MMCR reflectivity profiles for model validation and to retrieve cirrus microphysical properties, and V_D to determine "in-cloud" mesoscale vertical velocity (described in section 4.2).

2.3. Radar-Lidar Retrieval of Cloud Microphysical Properties

[12] The ice water content (IWC) and effective radius (r_{eff}) of upper tropospheric clouds can be retrieved by combining the RL extinction and MMCR reflectivity profiles using the technique of *Wang and Sassen* [2002a]. Microphysical properties retrieved using this lidar-radar algorithm have been compared extensively with aircraft measurements [*Wang and Sassen*, 2002a] and used to derive long-term statistics of cloud properties at the ACRF SGP site [*Wang and Sassen*, 2002b]. This algorithm also participated in an intercomparison of 12 different ice cloud retrieval schemes as well as in situ measurements [*Comstock et al.*, 2007]. Since cirrus particles are composed of mixtures of different habits (i.e., bullet rosettes, plates, columns, etc.) that are difficult to discriminate without auxiliary measurements (i.e., in situ particle imagers), the algorithm assumes that the ice crystal shapes are randomly oriented hexagons and that the PSD is a modified gamma distribution [i.e., *Mace et al.*, 1998]. The lidar-radar algorithm utilizes the parameterizations of *Fu* [1996] to relate the α_{ext} and Z_e with the IWC and generalized effective size (D_{ge}):

$$\alpha_{ext}(z) = IWC(z)\left(a_o + \frac{a_1}{D_{ge}(z)}\right) \quad (3)$$

and

$$Z_e(z) = C' \frac{IWC(z)}{\rho_i} D_{ge}^b(z) \quad (4)$$

where C' is related to the ratio of the dielectric constants of ice over liquid water, ρ_i is the density of ice, and a and b are fit coefficients. The parameter D_{ge} is defined as the ratio of the volume to surface area of a hexagonal ice crystal taking into account the aspect ratio of the crystal [see *Fu*, 1996]. Equations (3) and (4) are solved simultaneously using an iterative process provided that measurements of α_{ext} and Z_e are available. According to *Wang and Sassen* [2002a], a 100% error in Z_e/C' causes less than 20% error in IWC and D_{ge}. On the other hand, a 50% error in α_{ext} produces a 40% error in IWC. Therefore it is crucial to have accurate α_{ext} measurements. The ACRF RL α_{ext} measurement during the case examined in this paper has nearly 80% of in-cloud points with a random error <10%. This accuracy is sufficient for the IWC and D_{ge} retrievals, and would not be achieved using conventional single wavelength elastic scattering lidar. With the exception of a short time period (~0500–0520 UTC) the lidar penetrates the full vertical extent of the cloud. Typically, lidar signals become attenuation limited when the optical depth approaches 3. For comparison with model output, D_{ge} is converted to effective radius, r_{eff}, using the relationship $r_{\text{eff}} = (\sqrt[3]{3}/8) D_{ge}$ [*Fu*, 1996] assuming hexagonal columns.

2.4. SGP Large-Scale Forcing Data

[13] We force the cloud model using large-scale vertical velocity and advective tendencies derived as part of the Constrained Variational Analysis (CVA) product produced by the ARM program [*Zhang and Lin*, 1997; *Zhang et al.*, 2001]. The CVA product is produced by combining a network of radiosonde profiles (winds, temperature, and water vapor mixing ratio) from boundary facilities located around the ACRF SGP site. State variables are adjusted within their uncertainties such that mass, water vapor, heat, and momentum are conserved. An updated version of the CVA product is now available that uses Rapid Update Cycle upper air data and is constrained by surface observations and satellite data. The CVA data product is freely available on the ARM Web site (http://www.arm.gov) and has been evaluated extensively [*Xie et al.*, 2003, 2004].

3. Model Description

[14] We use the one-dimensional (1D) time-dependent cirrus model with size-resolved microphysics described by *Lin et al.* [2005]. We have made several adjustments to the original version in order to couple the model with the ARM CVA data. This type of coupling approach has been reported by others; e.g., *Khvorostyanov et al.* [2001] for the study of Arctic altostratus and cirrus clouds. In this version of the model, the prognostic variables are the dry static energy, $s = C_pT + gz$, the water vapor mixing ratio, q_v, the number concentration of aerosol particles per bin, and the number concentration for each ice crystal size bin, N_k. The mean water mass for each aerosol bin and the mean ice mass for each ice bin are also prognostic. Furthermore, the current model is able to treat the direct radiative effect on the growth of particles. We estimate the optical properties of ice crystals for a given PSD from first principles using an optical table for individual ice crystals derived from a database of the ice crystal scattering properties in the infrared wavelengths developed by *Yang et al.* [2005]. We also incorporate the heterogeneous nucleation scheme developed by *Khvorostyanov and Curry* [2004] (*KC04* hereafter). Details of the model updates are reported in the following sections.

3.1. Governing Equations

[15] The governing equations are

$$\frac{\partial s}{\partial t} = -\vec{V}\cdot\nabla s + s\frac{\partial\omega}{\partial p} - \frac{\partial\omega s}{\partial p} - \frac{\partial\overline{\omega' s'}}{\partial p} + \left.\frac{\partial s}{\partial t}\right|_{RAD} + \left.\frac{\partial s}{\partial t}\right|_{LH}, \quad (5)$$

$$\frac{\partial q_v}{\partial t} = -\vec{V}\cdot\nabla q_v + q_v\frac{\partial\omega}{\partial p} - \frac{\partial\omega q_v}{\partial p} - \frac{\partial\overline{\omega' q_v'}}{\partial p} + \left.\frac{\partial q}{\partial t}\right|_{PC}, \quad (6)$$

$$\frac{\partial N_k}{\partial t} = N_k\frac{\partial\omega}{\partial p} - \frac{\partial\left(\omega + g\rho_0 V_{T,k}\right)N_k}{\partial p} - \frac{\partial\overline{\omega' N_k'}}{\partial p} + \left.\frac{\partial N_k}{\partial t}\right|_{NUC} + \left.\frac{\partial N_k}{\partial t}\right|_{DIFF} + \left.\frac{\partial N_k}{\partial t}\right|_{AGG}, \quad (7)$$

where $\vec{V}$ is the horizontal wind, and the subscripts RAD, LH, PC, NUC, DIFF, and AGG denote radiative heating, latent heat release, phase change, nucleation, diffusional growth/decay, and aggregation, respectively. The K-theory is used to describe the turbulent flux of any prognostic variable A, such that $\overline{\omega' A'} = -\rho_0^2 g^2 K_e \frac{\partial A}{\partial p}$. At the domain boundaries, it is assumed that $\frac{\partial^2 A}{\partial p^2} = 0$, and $\frac{\partial\overline{\omega' A'}}{\partial p} = 0$.

[16] The CVA forcing product contains records of $\vec{V}\cdot\nabla s$, $\vec{V}\cdot\nabla q_v$, and ω in 25-mbar increments at 1-hour temporal resolution. To obtain their values at a given model time and pressure level, we first linearly interpolate the data temporally, and then use a cubic spline to interpolate the vertical profile to the appropriate pressure level. The pressure gradient of ω, $\frac{\partial\omega}{\partial p}$, is calculated by a second-order central difference scheme using the interpolated ω profile in the model domain and is treated as a known quantity when numerically integrating equations (5), (6), and (7) forward in time.

[17] A two-stream radiative transfer scheme [*Toon et al.*, 1988] is used to obtain the radiative fluxes and heating rates. The module contains 16 narrow bands between 4.546–62.5 μm. The k-distribution method [*Stephens*, 1984] is used to treat gaseous absorption by CO_2, water vapor, and O_3. Since in this study we are simulating a cirrus cloud observed during nighttime, we do not include solar radiative transfer in the computations.

3.2. Optical Properties of a Given Particle Size Distribution

[18] It is desirable for a cloud model with a capability of resolving PSDs to compute the optical properties of the resolved PSD in a consistent manner; that is, without introducing an intermediate parameter such as the effective radius. *Yang et al.* [2005], using the finite-difference time-domain method and an improved geometric optics method on the basis of the composite approach of *Fu et al.* [1998], have published an extensive optical property database for ice crystals of various distinct shapes. This database has been incorporated into the 1D cirrus model with some averaging procedures because the bandwidth of our radiative transfer module is larger than the database.

[19] The averaging formula is as follows [*Baum et al.*, 2005]:

$$\overline{Q}_{abs,i}(D) = \frac{1}{(\lambda_{i+1} - \lambda_i)}\int_{\lambda_i}^{\lambda_{i+1}} Q_{abs}(D,\lambda)\frac{B(\lambda)}{\bar{B}_i}d\lambda, \quad (8)$$

where λ is the wavelength, Q_{abs} is the absorption efficiency in the optical table, $\overline{Q}_{abs,i}$ is the absorption efficiency for the ith band in the model ($\lambda_i < \lambda < \lambda_{i+1}$), B is the Planck function, $\bar{B}_i$ is the averaged value within the wavelength interval, and D is the maximum dimension of the particle. Results of sensitivity tests of equation (8) on temperature indicate that $\overline{Q}_{abs,i}$ is not sensitive to temperature within the usual atmospheric range. Therefore we set temperature to 240 K in all the averaging procedures to obtain $\overline{Q}_{abs,i}$. The volume absorption coefficient of a model simulated particle size distribution is then obtained using $\overline{\sigma}_{abs,i} = \rho_a\sum\overline{Q}_{abs,i}(\bar{D}_k)A_kN_k$, where A is the geometric cross section of the particle, $\bar{D}_k$ is the maximum dimension derived from the mean ice mass of the bin number k, and ρ_a is air density.

[20] The cirrus model has an option to include scattering. If scattering is considered, the scattering efficiency is obtained as follows:

$$\overline{Q}_{sca,i}(D) = \frac{1}{(\lambda_{i+1} - \lambda_i)} \int_{\lambda_i}^{\lambda_{i+1}} Q_{sca}(D, \lambda) \frac{B(\lambda)}{\bar{B}_i} d\lambda, \tag{9}$$

and the volume scattering coefficient is obtained using $\overline{\sigma}_{sca,i} = \rho_a \sum_k \overline{Q}_{sca,i}(\bar{D}_k) A_k N_k$. The asymmetry factor ($g$) for ice particles at wavelength band i is computed using the following two equations:

$$\overline{g_i^*}(D) = \frac{\int_{\lambda_i}^{\lambda_{i+1}} g(D, \lambda) Q_{sca}(D, \lambda) B(\lambda)\, d\lambda}{(\lambda_{i+1} - \lambda_i)\bar{B}_i} \tag{10}$$

$$\overline{g}_i = \frac{\sum_k \overline{g_i^*}(\bar{D}_k) \bar{Q}_{sca,i}(\bar{D}_k) A_k N_k}{\sum_k \bar{Q}_{sca,i}(\bar{D}_k) A_k N_k} \tag{11}$$

The single scattering albedo for ice particles at wavelength band i is

$$\bar{\omega}_i = \frac{\bar{\sigma}_{sca,i}}{\bar{\sigma}_{abs,i} + \bar{\sigma}_{sca,i}}. \tag{12}$$

3.3. Direct Radiative Effects on the Diffusional Growth of Ice Crystals

[21] The net radiative power (in unit of energy per time), that is, the difference between the absorbed and emitted radiation by an ice crystal, may affect the heat transfer between the crystal and its environment and result in an enhancement or suppression of the particle growth rate. This direct radiative effect on the survival time of a single particle has been reported by *Hall and Pruppacher* [1976] and *Stephens* [1983], and later included in numerical cloud models [*Gu and Liou*, 2000; *Wu et al.*, 2000]. This work follows the theoretical framework described by *Hall and Pruppacher* [1976] and the procedure outlined in *Rogers and Yau* [1989, Chapter 7, p. 101] to approximate the relationship between $\rho_{vs}(T) - \rho_{vs}(T_r)$ and $T - T_r$, where T and T_r are the air and the ice particle surface temperature, respectively; and ρ_{vs} is the ice-saturation vapor density. In the derivation, the Clausius-Clayperon equation is used to compute the gradient of saturation pressure with respect to temperature. It can be shown that $T - T_r \approx -\left[\frac{\frac{R}{4\pi C} + LD'(S-1)\rho_{vs}(T)}{LD' \frac{\rho_{vs}(T)}{T}\left(\frac{L}{R_v T} - 1\right) + K'}\right]$. This term is then substituted into equation (7) of *Hall and Pruppacher* [1976], and the ice particle growth rate can be expressed by the following formulas:

$$\frac{dm_k}{dt} = \frac{4\pi C_k \left(S - 1 - \Delta S_{R,k}^*\right)}{\frac{L}{K_k' T}\left(\frac{L}{R_v T} - 1\right) + \frac{R_v T}{D_k' e_s}}, \tag{13}$$

where

$$\Delta S_{R,k}^* = \frac{1}{4\pi C_k K_k' T}\left(\frac{L}{R_v T} - 1\right) R_k, \tag{14}$$

m is the particle mass, C is the capacitance using electrostatic analogy, S is the saturation ratio with respect to ice, L is the latent heat of sublimation, T is the temperature, e_s is the saturation vapor pressure with respect to ice, R_v is the gas constant for water vapor, D' is the modified diffusion coefficient (considering the kinetic effect and the ventilation effect), K' is the modified thermal conductivity of air, R is the net radiative power (in units of energy per time) gained by the particle.

[22] $\Delta S_{R,k}^*$, the effective saturation ratio change with respect to ice due to radiative heat transfer, is caused exclusively by the net radiative power on the particle. It is clear that $\Delta S_{R,k}^*$ acts to enhance or suppress the "effective" supersaturation ratio. The net radiative power is formulated as

$$R_k = R_{abs,k} - R_{emit,k} = 4A_k \sum_i \bar{Q}_{abs,i}(\bar{D}_k) \cdot \left[\frac{1}{2}\left(F_i^+ + F_i^-\right) - \pi \bar{B}_i(\lambda_{i+1} - \lambda_i)\right], \tag{15}$$

where F_i^+ and F_i^- are the upwelling and downwelling fluxes for wavelength band i, respectively. As a consequence, if R is positive/negative (direct radiative heating/cooling), the growth rate is suppressed/enhanced.

[23] The magnitude of $\Delta S_{R,k}^*$ increases with particle size, as summarized in Tables 1 and 2 of *Hall and Pruppacher* [1976] for spheres and hexagonal columns in the maximum warming and maximum cooling conditions. In our study, the cloud optical depth is almost always smaller than 3 except for a few extreme runs. Furthermore, the ground temperature is about 4°C while the ground temperature is assumed to be 15°C in *Hall and Pruppacher's* calculations. Therefore it is expected that $\Delta S_{R,k}^*$ in our simulations is much smaller than those calculated using the maximum warming or cooling conditions. Those tables indicate that $\Delta S_{R,k}^*$ for the newly formed ice crystals at the top of this cloud should be much less than 0.01. As a result, the change in the diffusional growth rate is less than 2–3% (considering that the RHI in the nucleation zones is greater than 130%). Such a small $\Delta S_{R,k}^*$ is equivalent to a very small change in the deposition coefficient. Past studies have indicated that small changes in deposition coefficient do not affect N_i much [*Lin et al.*, 2002; *Gierens et al.*, 2003]. Thus it is expected that the direct radiation effect does not affect the nucleation pockets located near the top of the cloud much. Nevertheless, the direct radiative effect is likely to enhance the evaporation of larger ice crystals in the lower-half of the cloud moderately. We have conducted a sensitivity test on direct radiative effect on particle growth and find that the effect on cloud evolution and distribution of microphysical properties is minimal.

3.4. Heterogeneous Ice Nucleation

[24] *Khvorostyanov and Curry* [2000] and *KC04* have extended the classical theory of immersion and deposition heterogeneous freezing nucleation (e.g., chapter 9 of

Table 1. Summary of Tunable Parameters in the KC04 Heterogeneous Nucleation Scheme

Symbol	Description	Value	Reference
ε	elastic misfit strain	0 (dissimilar)	
		0.01–0.05	KC04, p. 2679
		0.01–0.02	KC2005
m_{is}	contact or wettability	1, the water wets the solid completely	KC2005, p. 264
	parameter	$0.4 \leq m_{is} \leq 0.67$, from sensitivity tests	KC2005, p. 264
	wetting coefficient	0.62–0.73 for quartz, beach sand	PK97, Table 5.2, p. 136
	compatibility parameter	0.42 Arizona Test Dust	*Marcolli et al.* [2007]
α	fraction of surface with m_{is} = 1	2×10^{-4}, 2×10^{-5}	tested in PK97
		2×10^{-6}	tested in KC2005

Pruppacher and Klett [1997]; *PK97* hereafter) to account for additional enhancement of the critical germ radius (r_{cr}) due to the solution effect and the elastic misfit strain (ε) between the ice and substrate lattice. The parameter ε accounts for the strain within an ice germ between the ice lattice and substrate lattice [*PK97*, Ch. 9]. The critical germ radius is then:

$$r_{cr} = \frac{2\sigma_{is}}{\rho_i L_m^{ef} \ln\left(\frac{T_0}{T}\right) S_w^G - C_\varepsilon \varepsilon^2 - \frac{r_{sc}}{r_d}} \tag{16}$$

where σ_{is} is the surface tension at the solution-ice interface, L_m^{ef} is the molar effective latent heat of melting, S_w is the water saturation ratio, C_ε is a constant related to the elastic misfit strain, r_{sc} is a scaling radius, and r_d is the radius of an aqueous solution drop or cloud drop. Equations for the dimensionless term G and the scaling radius r_d can be found in *KC04*. The critical energy of a germ formation is [*PK97*, equations 9–40]

$$\Delta F_{cr} = \frac{4\pi}{3} r_{cr}^2 \sigma_{is} f(m_{is}, x) - \alpha r_N^2 (1 - m_{is}), \tag{17}$$

where the wettability parameter (m_{is}) is equivalent to the cosine of the contact angle at the solution-ice interface and the abundance of active nucleation sites are considered, and r_N is the radius of the insoluble substrate and α is the fraction of surface with m_{is} = 1. Analogously, for deposition nucleation, ΔF_{cr} can be computed following arguments in *PK97* where σ_{is} and m_{is} are replaced with their ice-vapor equivalent σ_{iv} and m_{iv}, which represent the surface tension and wettability parameter at the vapor-ice interface, respectively.

[25] The nucleation rate is formulated as [*PK97*, equations 9–37]

$$J = \frac{B_z T}{h} c_{1s} 4\pi r_N^2 \exp\left[-\frac{\Delta F_{act}(T)}{B_z T} - \frac{\Delta F_{cr}}{B_z T}\right] \tag{18}$$

where B_z is the Boltzmann constant, h is the Planck's constant, $c_{1,s}$ is the concentration of water molecules adsorbed on 1 cm^2 of surface area, and ΔF_{act} is the activation energy at the solution-ice interface, and ΔF_{cr} is the critical energy of germ formation. The activation energy (ΔF_{act}) is based on limited laboratory and aircraft measurements of nucleation rates and is computed using a temperature-dependent expression similar to that reported by *Jensen et al.* [1994] for T ≤ -40°C and a linear fit similar to that of *Pruppacher* [1995] for T > -40°C. The actual values of parameters ε, m_{is}, and α are not well known. Table 1 summarizes their values from the literature. This heterogeneous nucleation scheme has been used to study thin cirrus clouds during CRYSTAL-FACE, where a sensitivity analysis was performed on ε and m_{is} [*Khvorostyanov et al.*, 2006]. Our model treats this type of ice nuclei as substance embedded in aqueous haze particles, which is a prognostic and binned species in the model.

[26] The cloud model has options to include either the KC04 nucleation scheme or a parameterized heterogeneous nucleation scheme of *Meyers et al.* [1992] (M92 hereafter), and also includes a switch to turn on, or off, the homogeneous nucleation scheme. The M92 parameterization represents a combination of deposition and condensation freezing and is based on observations of ice concentrations using a continuous flow diffusion chamber in orographic clouds over mountainous terrain. The nucleation parameters in M92 were originally derived from data collected at $-7° < T < -20$°C and 2% < RHI < 25% but has been applied to temperatures outside this range. It features a small activation RHI. In comparison, the activation RHI of KC04 is much higher. For example, at T = -45°C, the freezing nucleation rate for particles with r_N = 0.46 μm is 1 s^{-1} when RHI $\sim$ 139% (calculated with parameters listed in Table 2). Furthermore, the particle formation rates of the two schemes differ greatly right after nucleation: M92 features a small rate whereas KC04 a much greater rate. The aforementioned differences may result in differences in the number of ice

Table 2. Parameters Used in the Model Simulations Except as Noted in the Text and Table 3

Advection time step	5 s
Microphysics time step	0.1 s
Vertical resolution	~0.39 mbar
Nucleation mechanisms	Homogeneous (HOM): *Sassen and Dodd* [1988]; *Heymsfield and Miloshevich* [1993]; parameterized heterogeneous (HET-M92): *Meyers et al.* [1992]; classical theory heterogeneous (HET-KC04): *Khvorostyanov and Curry* [2000, 2004]
Deposition coefficient, α_D	0.006 or 1.0
Radiation	On
Aggregation	Off
Ice crystal shape	Hexagonal columns
Sulfuric acid drop concentration	200 cm^{-3}
Classical Theory Heterogeneous Nucleation Parameters	
Elastic misfit strain (ε)	0.025
Wettability parameter (m_{is})	0.6
Surface fraction (α)	0.5e-5
Ice nuclei concentration	0.02 cm^{-3} [*DeMott et al.*, 1997; *Haag and Kärcher*, 2004]

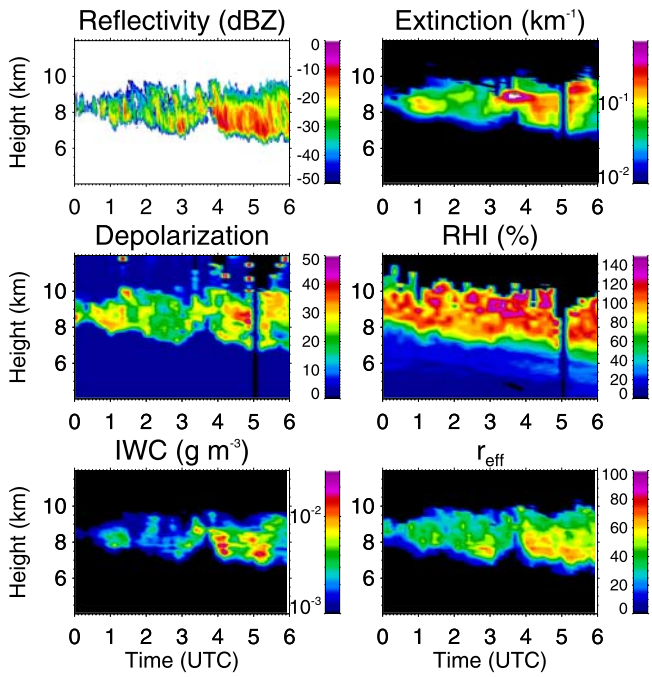

Figure 1. (a) Height vs. time display of radar reflectivity in dBZ, (b) Raman lidar extinction coefficient in km^{-1}, (c) depolarization ratio in %, (d) RHI in %, (e) retrieved IWC in g m^{-3}, and (f) r_{eff} in μm observed on 7 December 1999 at the ARM SGP site.

particle nucleated and the spatial distributions of N_i and RHI. Our model treats this type of ice nuclei as a prognostic and binned species by its own. These IN move with air and are removed when their corresponding activation RHI is achieved. The impact of nucleation mechanism is further investigated in section 4.2.4.

4. Model Simulations

[27] In this paper we examine a cirrus event observed on 7 December 1999, which corresponds to the initial approach of a frontal system associated with a weak upper level trough. MMCR and RL observations indicate that cirrus clouds advect over the site for ~8 hr with what appears to be three pulses. We will examine the first two pulses that occur between 0000 and 0345 UTC and 0345 and 0600 UTC (Figure 1). The average lidar derived optical depths for the two pulses are 0.6 and 0.9 indicating that the cirrus is becoming progressively thicker over the SGP site, which is typical for midlatitude cirrus related to synoptic phenomena. The MMCR reflectivity also increases as the cloud evolves, indicating an increasing presence of large particles. The RL derived q_v profiles reveal small patches of large ice supersaturation near cloud top (RHI ~ 130–150%), with moderate supersaturated regions (<120%) in the middle of the cloud and sub-ice saturation conditions near cloud base. We attempt to simulate the cirrus observed during this six hour period in Figure 1.

[28] To initialize the model, we use radiosonde data (pressure and temperature) and Raman lidar q_v measurements to derive the initial thermodynamic and moisture profile. The model is initialized using data obtained at 0000 UTC on 7 December 1999, which corresponds with an SGP radiosonde launch. The cloud top temperature (at 10 km) is −53°C. Gradients in potential temperature (θ) indicate that the cirrus layer is stable ($d\theta/dz > 2°C\ km^{-1}$). Since unstable cirrus cloud layers ($d\theta/dz < 0$) typically indicate convective regions (i.e., generating cells) [*Gultepe and Starr*, 1995], the stable conditions in this cloud implies that the structure in the layer is likely due to other dynamic mechanisms, such as gravity waves or pre-existent water vapor variability in the upper troposphere (Figure 2c). Wind directional shear is small (not shown). According to the vertical velocity data provided by the CVA product, the atmosphere is under conditions of weak large-scale ascent and increases slightly during the observation period (Figure 2d). We compare the derived RHI profile using q_v from both the radiosonde and RL measurements (Figure 2b) and find that the radiosonde is moister below cloud base than the RL profile, and is characterized by a nearly constant profile (ranging between 90–100%) in the cloud layer before gradually decreasing below cloud. The RL derived RHI profile is much more peaked with a RHI maximum almost exactly at cloud top of roughly 130%. There is a known water vapor dry bias in the Vaisala RS-80 radiosondes at cold temperatures used at the SGP site during this time period [*Miloshevich et al.*, 2001]. Simulations using the radiosonde q_v profile (not shown), with similar parameters to the large-scale runs presented in section 4.1, require unrealistically large vertical velocity to initiate cloud formation and produces unreasonable cirrus properties. Therefore we only report simulations using the RL q_v profile.

[29] Essential parameters for the control run are listed in Table 2. We choose the value for $m_{i,s}$ to be consistent with those measured for quartz or mixed composition (as reported by *Khvorostyanov and Curry* [2005]), and ε based

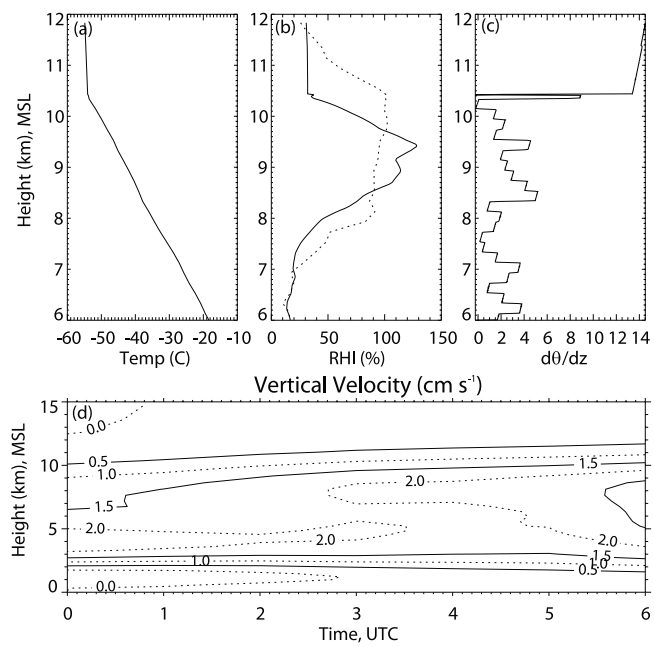

Figure 2. Vertical profiles of (a) radiosonde measured temperature (°C), (b) radiosonde and lidar measured RHI in %, (c) $d\theta/dz$ (°C/km), and (d) large-scale vertical velocity in cm s^{-1} obtained from the ARM constrained variational analysis product.

Table 3. Summary of Individual Simulations

Run	Vertical Velocity Forcing	Deposition Coefficient α_D	Nucleation Mechanism
L0-Fst	Large-scale	1.0 (fast growth)	HOM
L2-Fst	Large-scale +2 cm s^{-1}	1.0	HOM
L4-Fst	Large-scale +4 cm s^{-1}	1.0	HOM
L0-Slw	Large-scale	0.006 (slow growth)	HOM
L2-Slw	Large-scale +2 cm s^{-1}	0.006	HOM
L0-Fst-KC04	Large-scale	1.0	HET-KC04 + HOM
L0-Fst-M92	Large-scale	1.0	HET-M92 + HOM
W-Fst	Waves + Large-scale	1.0	HOM
W-Slw	Waves + Large-scale	0.006	HOM
W-Fst-M92	Waves + Large-scale	1.0	HET-M92 + HOM
W-Fst-KC04	Waves + Large-scale	1.0	HET-KC04 + HOM
W-Slw-M92	Waves + Large-scale	0.006	HET-M92 + HOM

on the middle of the range reported in KC04. Each model simulation has identical initial profiles. Initially, we performed the simulations assuming that the cirrus is forced by a weak large-scale updraft. In section 4.1, we discuss the problems with these assumptions. In the remaining sections, we present and discuss simulations that are forced using mesoscale vertical velocity derived from radar Doppler velocity measurements.

4.1. Simulations Using Large-Scale Forcing

[30] The 1D model is forced in a similar manner as a single column model (SCM), thus for these initial simulations, we assume that the cirrus forms via large-scale ascent. This assumption is somewhat unrealistic because midlatitude cirrus are not necessarily correlated with large-scale ascent [*Mace et al.*, 1997, 2001], although cirrus occurrence can correlate with large-scale ascent when horizontal advection of condensate is weak [*Mace et al.*, 1995] and in updrafts induced by warm conveyor belts [*Spichtinger et al.*, 2005]. Some general circulation models currently use a combination of vertical velocity and turbulent kinetic energy [*Lohmann and Kärcher*, 2002] to diagnose number of ice particles, and/or a prognostic scheme that relates cloud fraction to a distribution function of total water [*Tompkins*, 2002; *Roeckner et al.*, 2006]. As a first approximation, we performed a number of simulations using the 1D model in the SCM framework assuming gentle ascent to initiate cloud formation. For all simulations, the horizontal advection of condensate is ignored, primarily because the information is unavailable and not well constrained. The neglect of horizontal advection of condensate has been identified as a major setback for single column models to simulate cirrus occurrence [*Luo et al.*, 2003]. The onset timing of the cirrus may not be duly simulated when neglecting this advection. However, it is expected that the model may capture the overall cloud development after some spin-up time if the key forcing terms are accurate.

[31] In our initial simulations (not reported here), we performed a number of sensitivity tests to understand the model response to changes in the input parameters. These tests included perturbations in vertical velocity, nucleation mechanism, deposition coefficient, haze particle solution concentration, ice crystal fall speed, radiation, and ice crystal shape. Here, we present the parameters that have the most significant impact on the simulated RHI and microphysical properties, which include deposition coefficient and vertical velocity. We also explore the effects of nucleation mechanism on simulated cloud properties. Model simulations are summarized in Table 3. We first present simulations assuming ice crystals form by homogeneous nucleation under conditions of large-scale ascent, and perturb the magnitude of the updraft and the deposition coefficient.

[32] Our approach for comparing model simulations with observations is as follows. First, the bulk properties (ice water path (IWP), optical depth (τ), r_{eff} and cloud thickness (Δz)) are examined to see if the simulation captures the overall development of the cirrus. IWP is directly affected by the magnitude of forcing and moisture field. Therefore a well simulated IWP is the first necessary condition for a reasonable simulation. The probability density functions (PDFs) of RHI, IWC, r_{eff}, radar reflectivity (Z_e), and lidar extinction (α_{ext}) over a 6-hour simulation (or observation), which roughly covers one and a half cycles of the observed cirrus episodes, are used to examine the simulated cloud microphysical structure. Therefore these PDFs contain information about the cloud initiation, growth, and decay phases, and have to be interpreted carefully. For example, the PDF of RHI in the cloudy region reveals the overall efficiency of the phase change. If the cloud is efficient in removing excess water vapor or replenishing subsaturated air, the PDF of RHI should be narrow but with a small tail to the threshold nucleation RHI and should have a peak at 100%. For the PDF comparisons, the model simulations are sub-sampled to agree with the detection limit of the instruments. Thus cloudy simulation points are removed when the $\alpha_{ext} < 10^{-3}$ km^{-1} and $Z_e < -60$ dBZ.

[33] Note that observations of ice crystal number concentration (N_i) are not available during this time period; therefore we will discuss N_i results in relation to those observed during previous midlatitude cirrus field experiments. We indirectly evaluate the validity of the PSD using a combination of Z_e and α_{ext} observations, which are computed directly from model PSDs assuming equivalent spheres for Z_e calculations and columns for α_{ext} (to stay consistent with the ice crystal shape assumed in the cloud model simulations). To compute α_{ext}, we use the scattering properties database derived for wavelengths 0.2–5.0 μm [*Yang et al.*, 2000] to obtain the extinction cross section at 355 nm, which is consistent with scattering properties used in the cloud model. We also take into account atmospheric attenuation in the simulated Z_e and α_{ext} profiles. The quantities Z_e and α_{ext} are more sensitive to large and small particles, respectively. If the model can simulate the distribution of both quantities well (although the N_i and α_{ext} will be primarily driven by the small particle mode), then we can infer that the simulated PSD is reasonable.

4.1.1. Simulations Using Unperturbed or Uniformly Perturbed Large-Scale Forcing

[34] First, we compare the bulk properties simulated using the baseline CVA forcing data set (see Table 3 for the simulation naming convention) with observed quantities (Figure 3). The baseline large-scale forcing case (Run L0-Fst) grossly underestimates the bulk properties of the cloud indicating that either the large-scale forcing alone is too weak for the cloud development or horizontal advection (which we neglect) plays an important role in the cloud evolution. The large-scale forcing near 9.0 km varies from ~1.25 cm s^{-1} at the beginning of the simulation to

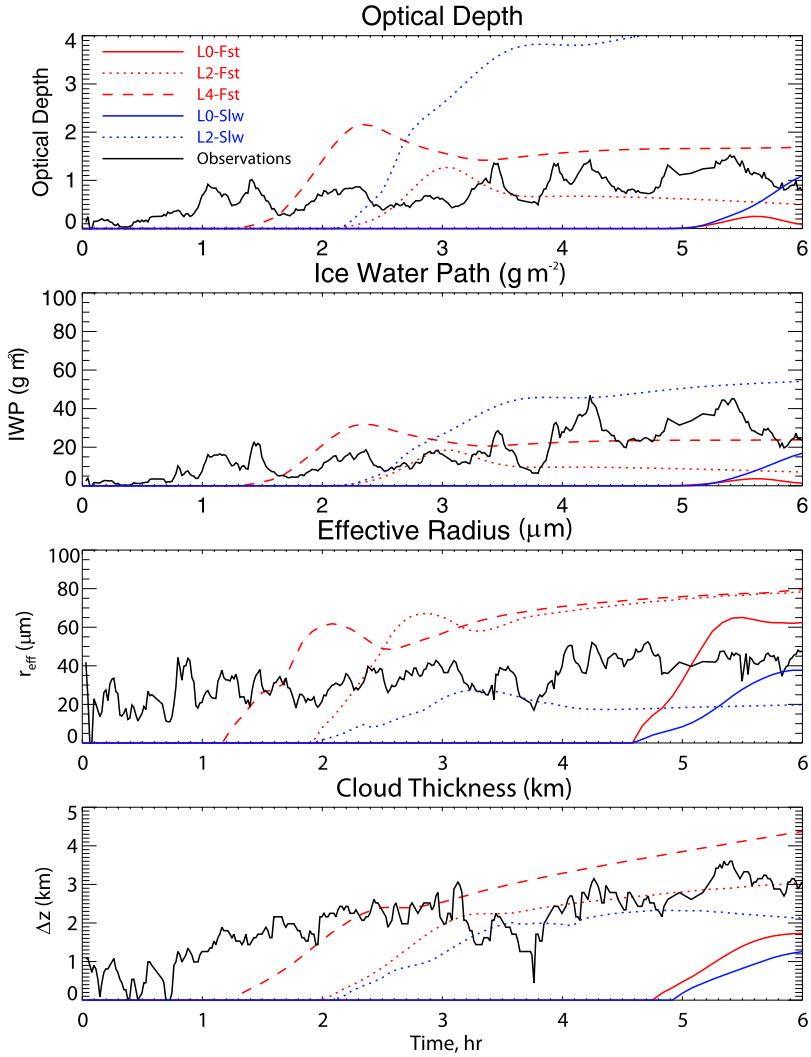

Figure 3. Time series of simulated bulk cloud properties compared with observations. Panels from the top represent visible optical depth, IWP (g m^{-2}), effective radius (μm), and cloud thickness (km) over the 6-hour simulation period.

~2.5 cm s^{-1} at the end of the simulation. By uniformly increasing the vertical velocity (Runs L2-Fst and L4-Fst), cloud initiation occurs earlier and comparisons with observations improve. In particular, the +2 cm s^{-1} case (Run L2-Fst) improved the comparison of τ, IWP, and Δz, although r_{eff} is overestimated. The +4 cm s^{-1} case (Run L4-Fst) overestimates all bulk properties with the exception of IWP, which is overestimated early in the simulation, then underestimated later.

[35] Although increasing the baseline large-scale vertical velocity improves the comparison of bulk properties with observations, its PDF comparison with the observations indicates problems. From Figure 4, both L2-Fst and L4-Fst have reasonable N_{i} ($1 < N_{\mathrm{i}} < 100$ L^{-1}) for updraft velocities of this magnitude [*Kärcher and Lohmann*, 2002] and the PDFs of IWC and α_{ext} compare well with observations. However, the PDFs of r_{eff} and Z_{e} compare poorly, where both L2-Fst and L4-Fst overestimate the occurrence of large r_{eff} and Z_{e} due to an overproduction of large particles.

[36] The effects of large-scale vertical velocity on simulated quantities may be deduced from Figures 3 and 4. A stronger uniform forcing prompts an earlier cloud initiation and increased ice particle production, which enhances the cloud's efficiency in phase change or deposition of water vapor (shifting the location of the mode of the PDF of RHI to smaller values). Stronger updrafts also produce a larger IWP and a deeper cloud due to cooling induced by increased vertical transport. Although the frequency of $r_{\mathrm{eff}} > 100$ μm increases with vertical velocity, the mean r_{eff} (Figure 3) is nearly the same and IWP increases because of higher ice number concentrations.

4.1.2. Deposition Coefficient

[37] Since we are also interested in testing the influence of particle growth rate on the simulated cloud properties and RHI evolution, we change α_{D} from 1.0 (fast crystal growth) to 0.006 (slow crystal growth). We choose the value $\alpha_{\mathrm{D}} = 0.006$ because this is the mean of the most recent laboratory measurements [*Magee et al.*, 2006]. Our sensitivity analyses (not shown) indicate that the simulated cloud properties do not change significantly until $\alpha_{\mathrm{D}} < 0.1$, consistent with *Lin et al.* [2002] and *Gierens et al.* [2003]. In Run L0-Slw ($\alpha_{\mathrm{D}} = 0.006$ and the model is forced by the

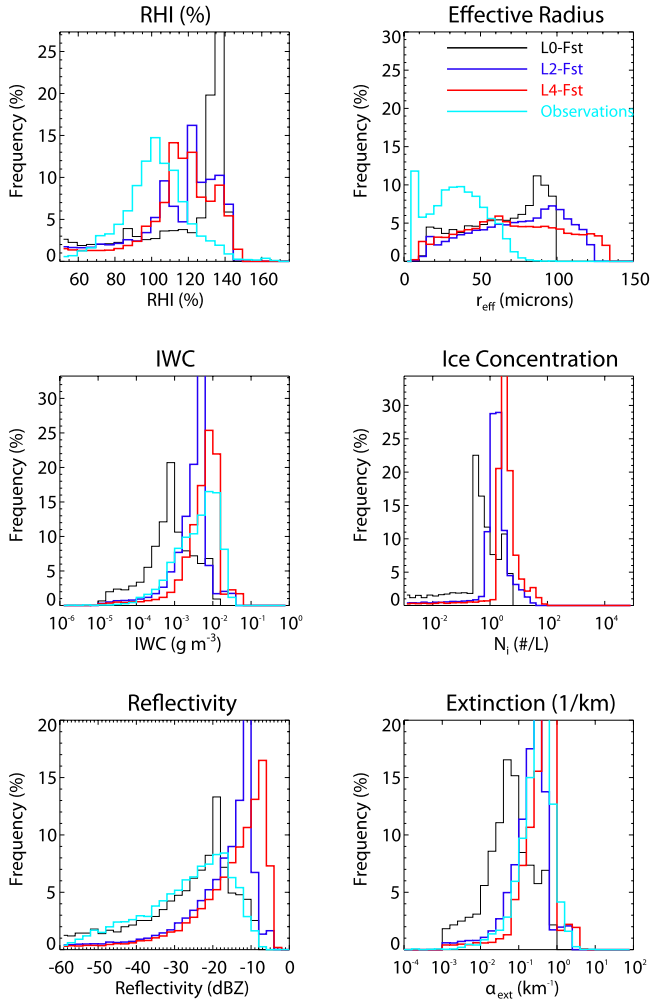

Figure 4. Frequency distributions of RHI (%), r_{eff} (μm), log(IWC) (g m^{-3}), log(N_i) (L^{-1}), Z_e (dBZ), and α_{ext} (km^{-1}) comparing the changes in model simulations due to increased large-scale vertical velocity (L0-Fst, L2-Fst, and L4-Fst) with observations. All simulations assume large-scale forcing and homogeneous nucleation.

baseline CVA data), the onset of cirrus formation takes place at around 4.5 hr, which is the same as Run L0-Fst. The simulated bulk properties do not improve significantly when changing α_D alone (L0-Slw), although the ice number concentration is higher and crystals are smaller, yielding a larger optical depth than the L0-Fst case.

[38] If we again assume α_D = 0.006 and in addition increase the vertical velocity by 2 cm s^{-2} (Run L2-Slw), the evolution of Δz is similar to L2-Fst, and the microphysical properties are comparably offset from observations (i.e., IWP and r_{eff}) but in the opposite direction (i.e., r_{eff} is smaller and larger than observations for L2-Slw and L2-Fst, respectively. When the α_D is reduced and vertical velocity increased (L2-Slw) the ice crystals are much smaller and optical depth correspondingly much larger (Figure 3).

[39] Alternatively, we compare frequency distributions of model simulated RHI, r_{eff}, IWC, Z_e, and α_{ext} with observations between 0000 and 0600 UTC for varying α_D (Figure 5). Note that from Figure 3, the number of time steps with cloud is much smaller for the L0-Fst and L0-Slw runs because cloud initiation is delayed significantly when compared with the observations and their PDFs do not cover statistics of one complete cloud cycle. When α_D = 1.0 (L0-Fst), only a few crystals form, quickly grow to large sizes (mode at $r_{eff} \sim 100$ μm), and sediment without uptaking significant amounts of excess vapor in their paths (RHI remains large 120–140%). When α_D is reduced to 0.006 (Run L0-Slw), more crystals form (N_i is more than a factor of 100 larger than in Run L0-Fst), r_{eff} is reduced, and the RHI is drawn down somewhat to values between 100 and 120%, although a strong peak near 140% remains.

[40] In order to explain the differences in RHI and microphysical properties with changes in α_D, we can look into the growth process of ice crystals. Ice crystal growth depends on processes such as vapor and heat diffusion surrounding an ice crystal and molecular-scale processes that determine the amount of vapor that is incorporated into the crystal lattice [*Wood et al.*, 2001]. In our numerical 1D model, we utilize the assumption that the diffusion growth rate of ice crystals is approximated by a spheroid using the electrostatic analogy and prolate approximation (see equations (13)–(14)). The manner in which water vapor molecules are incorporated into the crystal lattice is still

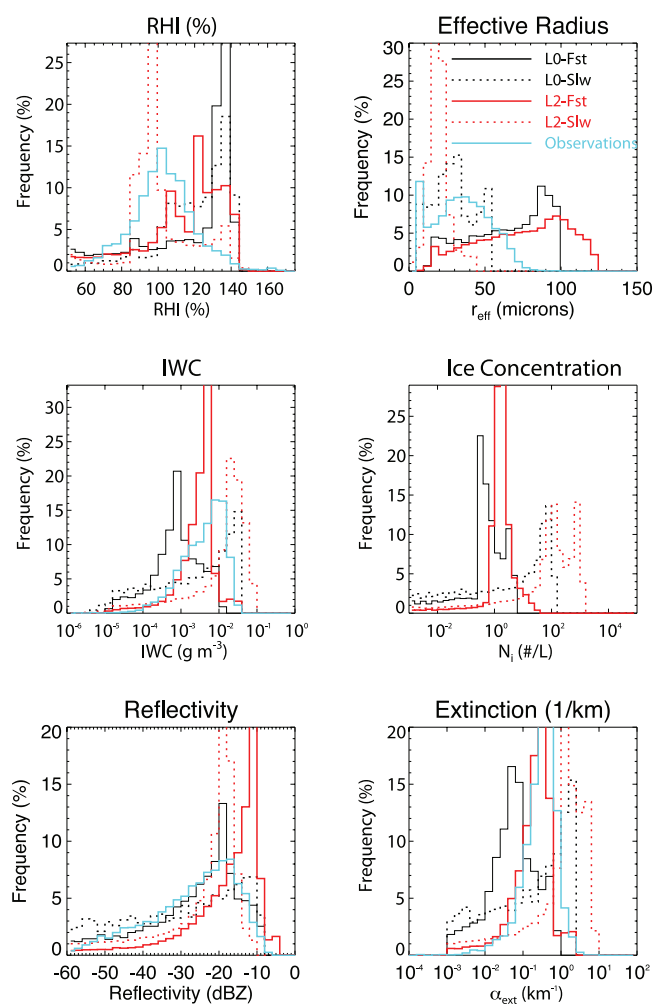

Figure 5. Same as in Figure 4 but comparing simulations with slow (α_D = 0.006) and fast (α_D = 1.0) ice crystal growth.

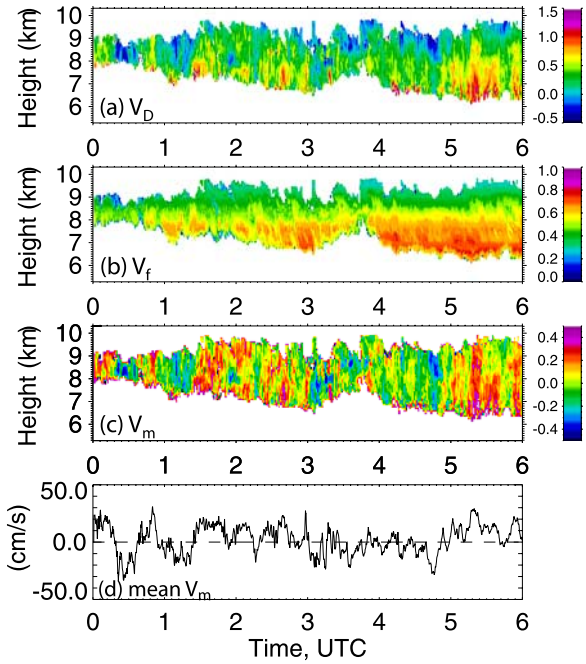

Figure 6. Height vs. time displays of (a) radar Doppler velocity in m s^{-1}, (b) retrieved ice crystal fall speed in m s^{-1}, (c) retrieved mesoscale velocity in m s^{-1}, and (d) vertical mean mesoscale velocity in cm s^{-1}. Note that, in each of these figures, positive values denote downward (toward the radar).

somewhat uncertain. One theory suggests that the crystal surface is composed of a series of flat areas that are partially covered with a series of ledges [*Wood et al.*, 2001]. These ledges grow as a result of water vapor molecules hitting the flat surface and skirting along this surface until they come in contact with an imperfection or "kink" in the ledges. The water vapor molecule attaches to the ledge at this point. Thus the crystal growth rate is related to the probability that the water vapor attaches to the crystal. The probability thus increases as the distance between ledges decreases. Furthermore, the size range in which the kinetic effect is effective depends on the value of α_D. For $\alpha_D = 0.006$, the kinetic effect may significantly reduce the growth rate of particles as large as 100 microns. The aforementioned discussion concerns the effect of α_D on the growth rate of an individual particle. The coefficient, however, will indirectly affect the number of ice crystals nucleated by altering the maximum RHI reached by the air parcel [*Lin et al.*, 2002]. The smaller α_D usually entails more ice particle production, which works to enhance vapor uptake of the population of particles in the air parcel. Therefore the gross effect of α_D on the efficiency of vapor uptake depends on which of the two mechanisms prevails.

[41] Since L0-Fst and L0-Slw do not cover one complete cycle of cirrus, we focus on comparing the L2-Fst and L2-Slw simulations. From Figure 5, L2-Slw produces a factor of 100–1000 more crystals than L2-Fst so that there is a much larger total surface area available for water vapor molecules to attach onto the growing crystals. The effect of α_D on the increase in the total surface area dominates its effect on the reduction of individual growth rate. As a result, L2-Slw is more efficient in phase change. Figure 5 shows that, in L2-Slw, more vapor is integrated onto the crystal lattice increasing the IWC and the occurrence of high RHI is also significantly reduced.

[42] In summary, simulations driven by large-scale forcing alone do not produce satisfactory results. None of the 5 simulations discussed in this section were able to satisfactorily reproduce the observed bulk properties and PDFs of the selected parameters simultaneously.

4.2. Simulations Using Forced Mesoscale Waves

[43] Dynamic variability in the upper troposphere occurs on several scales. While large-scale ascent is often considered to be one of the primary mechanisms for cirrus formation, there is little correlation between cirrus occurrence and synoptic-scale motions (1–2 cm s^{-1} updraft; ~100–200 km length) [*Mace et al.*, 1997, 2001]. Mesoscale variability (10–20 cm s^{-1} updraft; 10–100 km length) has been linked to cirrus formation and microphysical properties in a number of studies [*Gultepe and Starr*, 1995; *Kärcher and Ström*, 2003; *Sassen et al.*, 2007], and turbulence is found to have a significant role in the maintenance and dissipation of cirrus clouds [*Gu and Liou*, 2000].

[44] As mentioned previously, the 1D model essentially runs as a Single Column Model where large-scale ascent is the primary mechanism for cirrus formation. In all runs presented up to this point, the large-scale forcing from the ARM CVA data set is used to drive the vertical ascent in the model. In this section, we attempt to force the 1D model with mesoscale variability derived from radar Doppler velocity (V_D) measurements.

4.2.1. Determination of Mesoscale Velocity Variability

[45] The measured Doppler velocity (Figure 6a) includes both air and cloud motions. We assume that $V_D = V_{LS} + V_m + V_f$ where V_{LS} and V_m are the vertical air motions due to large-scale and mesoscale velocities, respectively. The ice crystal fall speed (V_f) is calculated using a method suggested by *Orr and Kropfli* [1999] (with variations applied by *Matrosov and Heymsfield* [2000] and *Mace et al.* [2002]). Our approach is similar to that of *Orr and Kropfli* [1999] such that V_f is determined using a conditional averaging approach where V_D is binned, then averaged, according to Z_e and altitude. If a particular altitude-Z_e bin has insufficient samples, we interpolate between bins with sufficient samples. It is assumed that each altitude-Z_e bin should represent volumes that contain similar PSDs and thus similar fall speeds. This method further assumes that if the samples of V_D in each altitude-Z_e bin are averaged, then the random turbulent motions are removed, and the mean V_D then represents the crystal fall speed (V_f; Figure 6b) for that population of ice crystals. We then compute the cloud mesoscale velocity ($V_m = V_D - V_{LS} - V_f$) for each radar profile (Figure 6c).

[46] The mean (vertically integrated) mesoscale velocity ($\bar{V}_m$) is also computed for each profile (Figure 6d). Since the retrieved vertically resolved V_m indicates that the direction of cloud vertical motions is usually the same throughout the vertical cloud extent (except during the 0300 to 0500 UTC time period), we assume that $\bar{V}_m$ represents the mean vertical updraft/downdraft in the cloudy column. Note that the average $\bar{V}_m$ over the 6 hour period is 2 cm s^{-1}.

[47] Although the retrieved values of V_f are somewhat larger than derived from aircraft measurements [i.e., *Mitchell*,

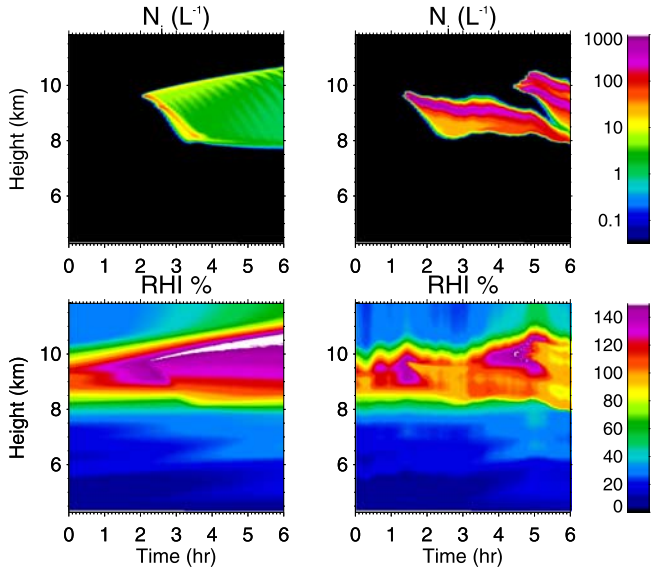

Figure 7. Simulated ice crystal number concentration (log(N_i) in L^{-1}) and RHI for L2-Fst (a and b) and W-Fst (c and d).

1996; *Heymsfield and Iaquinta*, 2000], we should note that the measured V_D is weighted toward the largest crystals in the radar volume and that a 500 μm particle would have a fall velocity of 70 cm s^{-1} using coefficients for columns reported by *Heymsfield and Iaquinta* [2000], which is the largest fall velocity derived for this case.

[48] The values for $\bar{V}_m$ in Figure 6 (±30 cm s^{-1}) are similar to those measured in previous aircraft based studies [*Gultepe and Starr*, 1995; *Quante and Starr*, 2002; *Kärcher and Ström*, 2003], who report updrafts in cirrus of 30–50 cm s^{-1}. Velocity between 30–35 cm s^{-1} was the primary velocity range that controlled ice number concentrations in the study of *Kärcher and Ström* [2003]. According to the work of *Orr and Kropfli* [1999], the absolute accuracy of this technique for determining $\bar{V}_m$ is <10 cm s^{-1}, when taking into consideration measurement precision, ground-clutter, antenna-pointing angle, etc. Note that in Figure 6, all velocity parameters are in terms of Doppler velocity, which means that positive values imply downward motion (toward the radar). We apply $\bar{V}_m$ to the 1D model by adding $\bar{V}_m$ to the background large-scale forcing profile every 5 seconds.

4.2.2. Variations With Vertical Velocity Forcing

[49] In this section, we compare simulations that force the 1D model using the measured mesoscale velocity variability with the large-scale forced case. Figure 7 displays the time evolution of the simulated cloud fields assuming α_D = 1.0 for both large-scale (L2-Fst) and mesoscale forced (W-Fst) cases. Since the 1D model does not account for certain dynamical interactions, such as in-cloud circulations driven by latent and radiative heating [*Starr and Cox*, 1985] and turbulence [*Gu and Liou*, 2000], these simulations are not able to capture detailed features of the cloud's evolution. However, it is clear that forcing the model with the mesoscale variability produces a much more realistic cloud evolution as compared with the large-scale forcing case. Previous work by *Kärcher and Ström* [2003] and *Jensen et al.* [2005] also find that mesoscale velocity, particularly gravity waves in the later study, are required to reproduce ice crystal number concentrations measured in cirrus clouds. When applying realistic velocity forcing, there are now two distinct "pulses" of cloud formation apparent, and the evolution of the RHI tends to mimic the behavior in the observed values (Figure 1d). Note the periods of enhanced RHI occur between 0100–0200, 0300–0400, and ~0430 UTC, which is nearly identical to times of enhanced RHI in the simulations (compare Figures 1d and 7d).

[50] Although W-Fst improves the simulation, the structure of the RHI of W-Fst differs from the observation. First, the moist layer extends downward from z = 8.5 km at 0000 UTC to z = 6.5 km at 0600 UTC in the observation whereas the downward development is less significant in the simulation. Second, in the W-Fst case, in-cloud regions of RHI = 80–100% extend from cloud base to cloud top and are associated with the mesoscale downdraft periods while, in reality, the moderate subsaturated regions are distributed in a more scattered fashion (Figure 1d). These two differences are associated with our application of $\bar{V}_m$ to the entire model domain and the inherent limitations of a 1D model. Furthermore, Lin et al. (unpublished manuscript) have found that significant sub-grid (relative to the CVA) horizontal moisture forcing exists in the lower part of this cloud, which may be the main cause of the downward development of the cloud.

[51] The simulated IWP and Δz for Run W-Fst (assuming α_D = 1.0) compare favorably with the observations (Figure 8). It is clear that the consideration of mesoscale waves has greatly improved the simulations of IWP and Δz as compared with the L0-Fst case (recall Figure 3). Run W-Fst obtains r_{eff} and τ with a magnitude comparable to the observed, except for the time period between 0450 and 0530 UTC when r_{eff} is smaller and τ is greater than observed. It is likely that the lidar derived optical depth (and cloud top height) is underestimated during this time period because the lidar signal is somewhat attenuation limited between 0500 and 0520 UTC, as is evident in Figure 1b.

[52] The pattern of the PDF of Z_e for the W-Fst case (Figure 9) is greatly improved as compared to the L2-Fst case, which is the best simulation among the large-scale ascent tests. The other PDFs for the W-Fst case are comparable to the observed, although their differences are not negligible. From the PDFs of r_{eff} and α_{ext}, the W-Fst case slightly over-estimates the production and occurrence of small particles.

4.2.3. Deposition Coefficient

[53] In a set of simulations similar to L0-Fst and L0-Slw (i.e., Figure 5), we again compare the fast and slow crystal growth cases, but with the addition of mesoscale wave variability (Runs W-Fst and W-Slw). For a first assessment of the simulations forced by mesoscale waves, we examine the evolution of the bulk properties (Figure 8). The simulated IWP and Δz for Run W-Fst (assuming α_D = 1.0) and W-Slw (assuming α_D = 0.006) are similar between 0110 and 0230 UTC. After 0230 UTC, the W-Fst produces slightly smaller IWP and Δz than W-Slw. Nevertheless, the IWP and Δz for these two Runs both compare favorably with the observations. Run W-Fst obtains τ with a magnitude comparable to the observed while Run W-Slw overestimates τ and underestimates r_{eff}, implying that the number of crystals is overestimated and the mean size is too small. The PDFs of r_{eff}, N_i, Z_e and α_{ext} support this deduction (Figure 9).

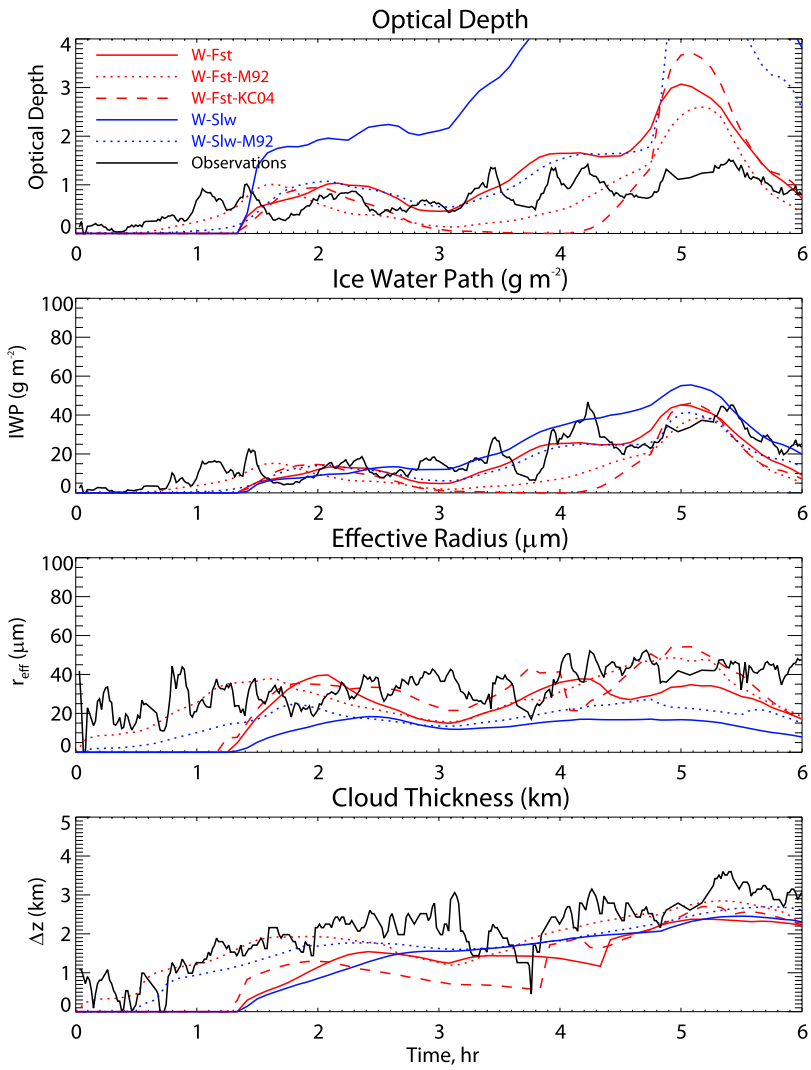

Figure 8. Same as Figure 3 but comparing simulations varying nucleation mechanism and ice crystal growth rate. These simulations use mesoscale wave forcing.

[54] The contrast between the PDFs of W-Fst and W-Slw is not significant (Figure 9), with the exception of N_i and to a lesser extent α_{ext} and r_{eff}. The primary differences are that W-Slw produces an enhancement in $N_i \sim 10^4$ L^{-1} that occurs in the nucleation zone. After nucleation is shut off, the vertical flux divergence of N_i is not significant because (1) many of them are nucleated at the same time thus evolving at the same pace and (2) the growth is slow because of vapor competition. The large number of crystals causes the r_{eff} and Z_e to be lower than the W-Fst case. The result is that we have a significant occurrence of small crystals (<10 μm) that creates a sub-peak in the α_{ext} near 10 km^{-1}, which is not observed in the lidar measurements.

[55] In addition, the W-Slw case produces an increase in the occurrence of RHI below 100% but a decrease in the occurrence of high RHI (Figure 9). The latter is caused by the increase in the efficiency in removing excess water vapor in the regions containing many ice particles. One naturally wonders why the efficiency in replenishing water vapor in the sub-saturated region is not enhanced. To answer this paradox, we should recall that the N_i distribution in the W-Slw case is bimodal (Figure 9). In the W-Slw case, $N_i > 10^3$ L^{-1} is limited to the upper portion of the cloud, and many cloudy volumes do not contain significant numbers of ice crystals. Given a PSD, the fast-growth mode is more efficient in phase change than the slow-growth mode. Consequently, a significant portion of the cloudy volumes are not as efficient in phase change and they can survive longer in downdrafts, producing an increase in the occurrence of RHI < 100% in the W-Slw case.

4.2.4. Nucleation Mechanism

[56] As discussed in the Introduction, it is conjectured that the nucleation mechanism may significantly impact the RHI and microphysical properties in the cloud and hence the radiative forcing. Although homogeneous nucleation is often assumed to be the dominant nucleation mechanism in cirrus, there is a potential for heterogeneous nucleation to contribute to ice formation if sufficient ice nuclei exist, especially if the vertical motion forcing is weak [*Lin et al.*, 2002]. We wish to demonstrate the effects of the nucleation mechanism on the simulated cloud properties by comparing the new KC04 scheme with the commonly used M92 formulation. Hereafter, we refer to homogeneous nucleation, parameterized heterogeneous nucleation [*M92*], and classical

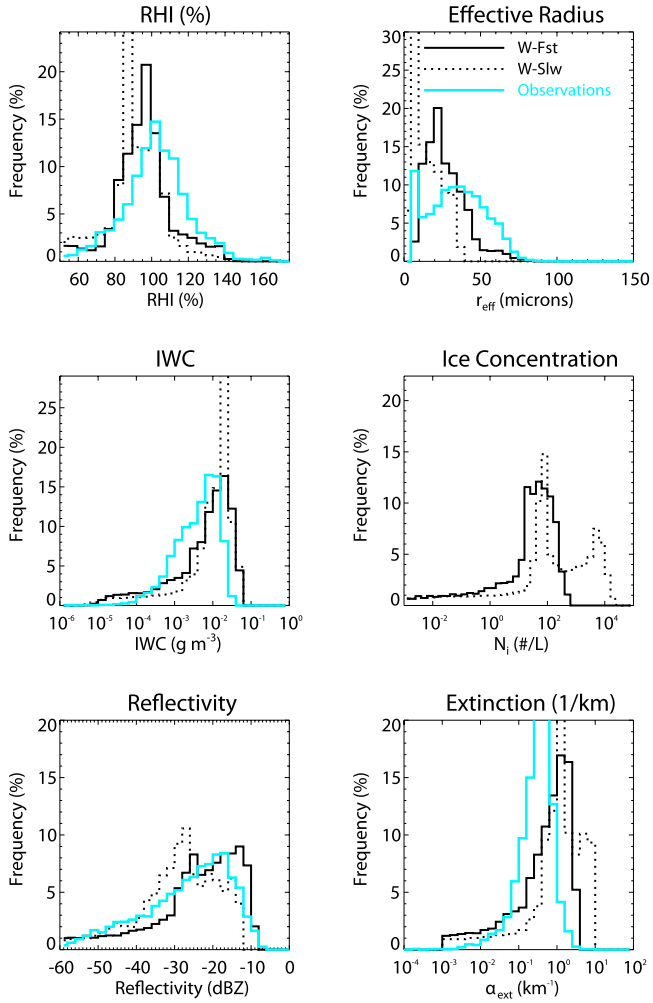

Figure 9. Same as Figure 4 but comparing the slow and fast ice crystal growth simulations. Both runs use mesoscale wave forcing.

theory heterogeneous nucleation [*Khvorostyanov and Curry*, 2000; *KC04*] as HOM, HET-M92, and HET-KC04, respectively. Note that in the HET-M92 and HET-KC04 simulations, both homogeneous and heterogeneous processes are allowed to occur. The homogeneous scheme is formulated using the references listed in Table 2.

[57] We first compare the bulk properties obtained by Runs W-Fst, W-Fst-M92 and W-Fst-KC04 (Figure 8). The peak IWP values of the two cirrus episodes are comparable among the cases although their evolution differs significantly especially between t = 3 and 4 hr. This significant difference likely results from the differences in the number of surviving particles in the meso-downdraft period (between t = 2 and 3 hr). Run W-Fst-M92 produces the most realistic cloud depth with respect to the observation while the other two simulations underestimate Δz slightly.

[58] In addition to nucleation mechanism, Figure 8 also demonstrates the effect of slow crystal growth for different nucleation mechanism. Note that W-Slw-KC04 is not shown in Figure 8 because the results are nearly identical to W-Slw; that is homogeneous nucleation dominates the W-Slw-KC simulation. We will discuss this point later in this Section. The results for W-Slw-M92 compare similarly to W-Fst-M92 with the exception that the former simulation produces smaller r_{eff} and larger τ due an increase in N_i for small crystals.

[59] Changes in the frequency distributions of simulated cloud properties due to changes in nucleation mechanism (Figure 10) are more subtle than changes due to velocity and α_D. Their differences are too small to shed light on the nucleation mechanism that is most likely to take place in reality. Nevertheless, the cirrus simulated by W-Fst features much greater N_i and smaller particles than W-Fst-M92 and W-Fst-KC04. Furthermore, significant differences are apparent in N_i and RHI where the occurrence of small values of N_i for W-Fst-M92 and W-Fst-KC04 is more frequent than for W-Fst; with the exception of a narrow secondary peak at ~500 L^{-1} for W-Fst-KC04. A secondary peak is also seen in the RHI distribution in Figure 10 for the W-Fst-KC04 case, which is caused by the fewer number of crystals that formed and subsequently uptake less water vapor overall (see discussion of Figure 11 below). The W-Fst-M92 case is in good agreement with nearly all observed parameters, including the lidar extinction. Note that N_i for Run W-Fst-M92 is always <100 L^{-1}, and is

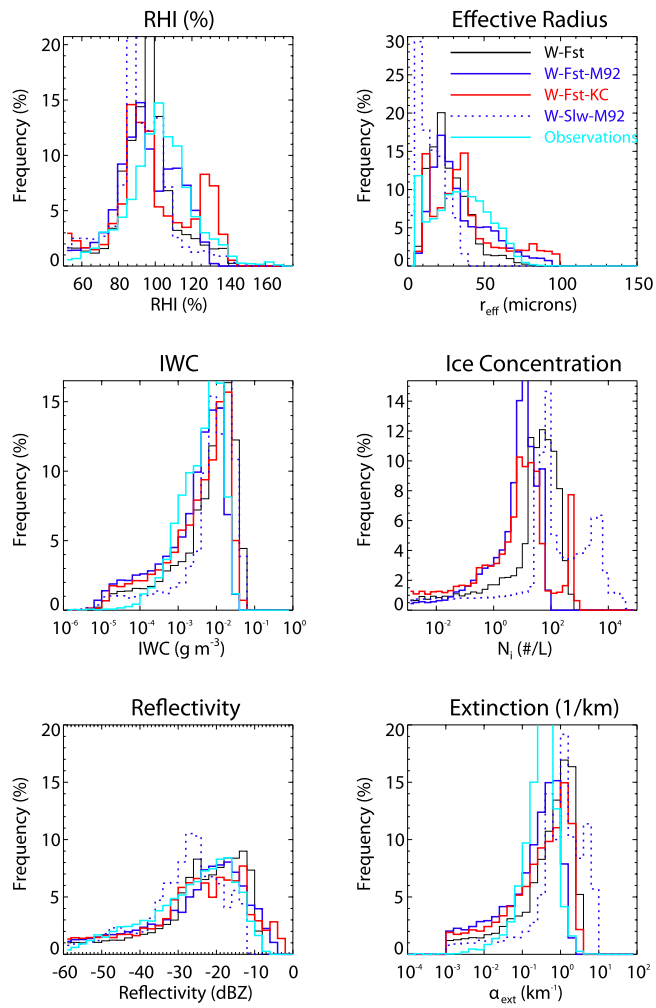

Figure 10. Same as Figure 9 but comparing simulations varying nucleation mechanism. These simulations also use mesoscale wave forcing.

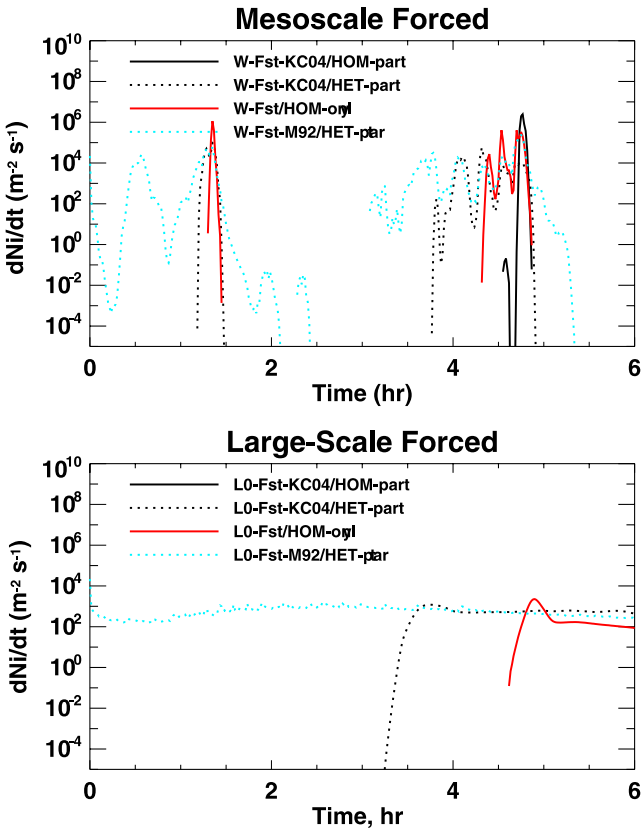

Figure 11. Time evolution of the number of ice crystals nucleated at each time step integrated vertically over each column in units of m^{-2} s^{-1}. For simulations that include both HOM and HET nucleation, we split N_i according to mechanism. Note that, for the W-Fst-M92 and L0-Fst-M92 runs, homogeneous nucleation was allowed but never initiated, and in the W-Fst and L0-Fst runs, only HOM was allowed to activate ice formation.

consistent with both the lidar α_{ext} and radar Z_e. Finally, the PDFs of W-Slw-M92 do not compare as favorably with the observations although its bulk properties were reasonable. The PDFs of W-Slw-M92 exhibits similar behavior to W-Slw in that the slow crystal growth increases N_i and decreases r_{eff} as noted in Figure 8.

[60] To understand the role of each nucleation mechanism in the simulations, the contribution of each nucleation mechanism to N_i is examined in Figure 11. As the figure denotes, competition between HET and HOM does not occur in any large-scale forcing (L0-Fst) cases and new crystals tend to form in the column continuously, predominantly near cloud top (Figure 7a) because the ascent is constant. W-Fst-KC04 is the only simulation in the wave (W-Fst) simulations that have both the HOM and HET modes activated. When the HET-M92 scheme is used, HOM nucleation is inhibited for both the large-scale and mesoscale forcing cases.

[61] Because of the higher ice supersaturation thresholds required for HOM, HOM occurs sporadically when the mesoscale forcing is included and generates many ice crystals over a few minutes when the threshold is reached as the wave peaks. In contrast, at any time step, the HET schemes typically produce fewer crystals than the HOM scheme, if it is activated. Integrating over the 6-hour simulation time, W-Fst-KC04 produces the most crystals (HOM = 6.0E + 6, HET = 7.8E + 5), with W-Fst and W-Fst-M92 producing significantly fewer crystals (3.8E + 6 and 2.0E + 6, respectively). Interestingly, homogeneous nucleation produces almost twice as many crystals during W-Fst-KC04 than in W-Fst, where only HOM is activated. This is because when (in W-Fst) the initial pulse (between 1 and 2 hr) is due to HOM rather then HET, dN_i/dt is larger, which increases the deposition of water vapor and suppresses the subsequent increase of RHI during the second pulse (between 4 and 5 hr). Essentially, during the second pulse, for W-Fst-KC04 virtually the entire layer has RHI > 120%, whereas for W-Fst only the uppermost portion of the layer has RHI > 120% (recall Figure 7d). Therefore, in the W-Fst-KC04 case there are more crystals nucleated by HOM because of higher water vapor availability. We should note that the prescribed ice nuclei (IN) in both HET schemes are prognostic variables in the model; i.e., they are tracked and are removed from the system when nucleated. During W-Fst-KC04 the assumed IN concentration is not fully depleted during the simulation as is evident in Figure 11 where HET continues to occur during the last pulse.

[62] For L0-Fst-KC04 (large-scale forced case; HET-KC04 plus HOM), the gentle updraft initiates the formation of ice via the heterogeneous mechanism at around t = 3.25 hr (Figure 11b; black dotted line). Since the RHI remains below the critical threshold, the homogeneous nucleation process is not initiated and there is a nearly constant production of ice via heterogeneous nucleation. In an analogous run, but forced with mesoscale waves (W-Fst-KC04) the HET-KC04 mechanism initiates first after ~1 hr (black dotted line; Figure 11a). Later in the simulation, HET is again initiated at ~3.5 hr, has a series of weak pulses, and then a final stronger updraft at around t = 4.75 hr, which allows HOM to occur as well. This last pulse due to homogeneous freezing is the source of the secondary peak in N_i seen in Figure 10 for the HET-KC04 case. The secondary peak in RHI for the HET-KC04 case (Figure 10) is caused by the smaller number of crystals nucleated by the HET-KC04 processes (as opposed to the HOM only case; solid red line in Figure 11). Essentially, in the W-Fst-KC04 case, smaller numbers of crystals form initially, uptake less water vapor than in the HOM-only case, and therefore the RHI remains larger (120–140%) during the 3.5 to 5.0 hr time period, which generates the secondary peak in RHI when the mesoscale updrafts increase.

5. Discussion and Conclusions

[63] We have presented a series of simulations to understand the sensitivity of the microphysical properties to changes in model parameters, and to understand factors that control the magnitude and evolution of the RHI. Many previous studies have used number concentration to validate cirrus model simulations [e.g., *Kärcher and Ström*, 2003; *Jensen et al.*, 1994]. Measurements of ice crystal PSDs vary widely, and concentrations of small crystals have been reported as large as 10^4 L^{-1} in wave clouds [*Heymsfield and Miloshevich*, 1995] and cirrus [*Gayet et al.*, 2002]. One problem with this approach is that aircraft measurements of

ice crystal PSD have undergone scrutiny from the community because of shattering of large crystals on probe inlets [*Field et al.*, 2003; *McFarquhar et al.*, 2007]. We instead use ground based observations of RHI, IWC, r_{eff}, α_{ext}, and Z_e to evaluate model simulations and estimate reasonable values for N_i. IWC and r_{eff} are derived using a combined lidar-radar algorithm, which takes into account contributions from both the large and small particle modes of the PSD. Although our simulations represent only one cirrus case, this case (with cloud top temperature $\sim -53°C$) is representative of cirrus clouds observed over North America based on statistical data sets [*Mace et al.*, 2001; *Sassen and Comstock*, 2001].

[64] We demonstrate the use of radar Doppler velocity measurements to assess the cloud-scale variability and directly force the model using the measurements. To our knowledge, direct use of the radar velocities in a cloud model has not been previously demonstrated. While we do not expect to accurately simulate the exact structure of the cloud evolution because of our neglect of turbulent-scale influences, we demonstrate that forcing the model with radar velocity estimates improves simulations of the evolution and magnitude of cloud bulk properties as well as the probability distributions of RHI and optical properties. Our findings suggest that the mesoscale velocity is the primary driver of the magnitude and evolution of the RHI, which is consistent with previous results [*Kärcher and Ström*, 2003; *Jensen et al.*, 2005; *Sassen et al.*, 2007]. To put our results in context with previous aircraft based results, the peak frequency of the N_i predicted in our model are two orders of magnitude smaller than observed by aircraft results used by *Kärcher and Ström* [2003], which were observed in young cirrus clouds over northern Europe. Our results for N_i are more consistent with cirrus models derived using *in situ* observations over North America including the ARM SGP site [*Nasiri et al.*, 2002] and a factor of 10 smaller than cloud particle imager (CPI) measurements also over North America [*Lawson et al.*, 2006]. The model intercomparison project associated with the Working Group 2 of the GEWEX (Global Energy and Water Cycle Experiment) Cloud System Study (GCSS) is also analyzing the influence of gravity waves on midlatitude cirrus.

[65] Nucleation mechanism appears to be a secondary driver as compared to the change in the forcing and deposition coefficient considered in this study. Nevertheless, our results suggest that (1) the HET-M92 scheme is quite reasonable in its prediction of the distribution of RHI and microphysical properties; (2) homogeneous nucleation tends to produce larger concentrations of small crystals (when mesoscale forcing is used), which results in larger α_{ext} and τ, and reduced RHI as compared with observations (see Figures 8 and 10); (3) the occurrence frequencies of moderate (100 to 120%) to high (>120%) RHI in HET-M92 and HET-KC04 schemes are greater than that produced by the homogeneous nucleation only run. This is also true for simulations using HET-KC04 *without* allowing HOM to occur (not shown). This finding suggests that if heterogeneous nucleation processes dominate in more polluted regions (as suggested by *Haag et al.* [2003]), the occurrence of in-cloud supersaturated regions >10% will be more frequent.

[66] In addition to the vertical velocity and nucleation mechanism, we also explored the effects of a small deposition coefficient on the simulations of cirrus properties. Our simulations show that decreasing α_D from 1 to 0.006 results in an increase of N_i by a factor of 100 in both the large-scale ascent and mesoscale forced simulations. When $\alpha_D = 0.006$ is assumed, we expect to see a significant increase in N_i, as well as a significant decrease in r_{eff} as seen by *Gierens et al.* [2003]. This result was reproduced in Figure 4 using large-scale forcing. However, when mesoscale forcing was used, N_i did increase, but the waves tend to "dampen" the effect (Figure 9). The largest N_i ($\sim 10^4$ L^{-1}) occurred when both mesoscale forcing and $\alpha_D = 0.006$ were used, although these were confined to the nucleation zone of the cloud, which was not observed in the remote sensing measurements. The simulations that are most consistent with remote sensing observations have number concentrations on the order of tens to hundreds of particles per liter, which is considerably less than the 10^4 L^{-1} measured by some aircraft probes.

[67] It is possible that uncertainty in the remote sensing measurements of Z_e and α_{ext} could influence the interpretation of these results. The uncertainty in the MMCR reflectivity measurements is at most 0.5 dBZ, but likely less because no significant attenuation is occurring on this day (the lower troposphere is relatively dry and there are no clouds below the cirrus). The lidar measurements could also be influenced by multiple scattering, which would cause an underestimation of the α_{ext}. However, when particles are small, photons tend to be scattered out of the lidar beam because forward scattering is reduced for small particles. We note that when $N_i \sim 10^4$ L^{-1} in the simulations, these are primarily small particles in the nucleation zone, and would be equivalent to $\alpha_{ext} \sim 10$ km^{-1}. The simulated nucleation regions where these large N_i are produced usually have vertical depths of $\sim$250 m, which is larger than the $\sim$78 m vertical resolution of the lidar measurements. Thus vertical averaging of the lidar data does not play a role in reducing the apparent value of α_{ext}. Since these large α_{ext} values are not measured at anytime during the 6-hour period, we argue that these large N_i likely do not exist for this case. We also note that analysis of several years of cirrus extinction measurements at SGP (not shown here, but to be reported in future work) is rarely larger than $\sim$5 km^{-1}.

[68] The simulated RHI and N_i could also be influenced by our assumption that the mean mesoscale velocity ($\bar{V}_m$) is uniform throughout the column over a 5-second time period. More realistically, Figure 6c suggests that although there are time periods when the velocity is relatively constant, there are also times when the profile oscillates between upward and downward motion. These turbulent motions would likely act to enhance or reduce the RHI and N_i in smaller pockets of air. Further analysis of the variability of both the RHI and V_m are warranted and could lead to further insight into the water vapor uptake rate in cirrus. In related work, we explore the potential for estimating water vapor uptake rate using Raman lidar water vapor and MMCR measurements to understand the sub-grid (relative to the CVA data) moisture forcing within cirrus clouds [*Lin et al.* unpublished manuscript].

[69] To further evaluate our conclusions, we recommend additional laboratory and field studies to help constrain assumptions in the model simulations and the measurements

used to evaluate the model. These studies should include: (1) laboratory studies to constrain heterogeneous nucleation parameters (i.e., misfit strain, contact angle, and surface active sites in Table 2) for typical upper tropospheric IN and to further understand particle growth rate, and (2) *in situ* airborne measurements to constrain the critical supersaturation threshold, characterize the ice nuclei and PSD in cirrus clouds, while concurrently measuring vertical motions. Sorting out the details of the PSD and microphysical properties of cirrus clouds and the dynamic processes that influence them is critically important in improving our understanding of cirrus radiative forcing and prediction of cirrus radiative feedbacks in global climate simulations.

Notation

A (1) Any prognostic variable in section 3.1 (2) Geometric cross section of a particle in other sections
a_0, a_1, b Fit coefficients in equations (3) and (4)
B Planck function
B_z Boltzmann constant
C Capacitance
C' A factor related to the ratio of the dielectric constant of ice over water (see equation 10 of *Wang and Sassen* [2002a])
C_L A factor related to RL calibration
C_p Specific heat of air at constant pressure
C_ε A constant related to the elastic misfit strain
$c_{1,s}$ The concentration of water molecules adsorbed on 1 cm^2 of surface area
D The maximum dimension of the particle
$\bar{D}_k$ The maximum dimension derived from the mean ice mass of the bin number k
D' Modified coefficient of diffusion of water vapor in air (considering the kinetic and the ventilation effects)
D_{ge} Effective size
e_s Saturation vapor pressure with respect to ice
F^+, F^- Upwelling and downwelling radiative fluxes, respectively
ΔF_{actv} Activation energy at the solution-ice interface
ΔF_{cr} The critical energy of a germ formation
g (1) Acceleration due to gravity except in equations (10) and (11). (2) The asymmetry factor in equations (10) and (11).
G A dimensionless factor
h Planck's constant
IWC Ice water content
J Rate of germ formation
K' Modified coefficient of thermal conductivity of air (considering the kinetic and the ventilation effects)
k A factor between 0 and 1 depending on the composition of the scatters (equation (1))
k_{lid} Constant containing laser pulse energy, receiver area, and channel sensitivity
K_e Eddy diffusion coefficient
L Latent heat of sublimation
L_m^{ef} Molar effective latent heat of melting
m Mass of a particle
m_{is} Wettability parameter at the solution-ice interface
n_j Number density of molecular species detected at wavelength j
N_k Number concentration of ice particles in size bin k (in number per mass of air)
N_{i} Number concentration of ice particles (in number per volume of air)
O Overlap function for lidar measurements
p Pressure
$q(\lambda_o, z)$, $q(\lambda_j, z)$ Transmission of the outgoing laser beam and backscattered signal, respectively
Q_{abs}, Q_{sca} Absorption efficiency and scattering efficiency, respectively
q_v Water vapor mixing ratio
R, R_{abs}, R_{emit} Net, absorbed, and emitting radiative powers of a particle, respectively
R_v Individual gas constant for water vapor
r_{cr} The critical germ radius in a solution droplet
r_{sc} Scaling radius
r_d Radius of the aqueous solution droplet
r_N Radius of the insoluble substrate
r_{eff} Effective radius
S, S_w Saturation ratio with respect to ice and water, respectively
ΔS_R^* Effective saturation ratio change with respect to ice due to radiative heat transfer
S_{387}, S_{408} Received Raman Lidar signals due to nitrogen and water vapor, respectively
s Dry static energy
T Temperature
T_0 273.15 K
t Time
$\vec{V}$ Horizontal wind
V_D Doppler velocity (positive values indicate downward motion)
V_{LS} Large-scale vertical velocity (positive values indicate downward motion)
V_m Mesoscale vertical velocity (positive values indicate downward motion)
V_f Fall speed of a population of particles
V_T Terminal fall speed of a particle
Z_{e} Radar reflectivity
z Altitude
Δz Cloud depth
α The fraction of surface with $m_{\mathrm{is}} = 1$
α_{ext} The particle extinction coefficient at 355 nm
α_{355}^{mol}, α_{387}^{mol} The extinction coefficients due to absorption and Rayleigh scattering at 355 nm and 387 nm, respectively.
α_{D} The deposition coefficient
ε The elastic strain between the ice and substrate lattice
λ Wavelength
λ_{355}, λ_{387} Wavelengths at 355 nm and 387 nm, respectively.

ρ_i, ρ_a Density of ice and air, respectively
ρ_0 Basic state air density (function of height only)
ρ_{vs} Saturation vapor density over ice
σ Raman cross section for molecular species
σ_{abs}, σ_{sca} Volume absorption coefficient and volume scattering coefficient, respectively
σ_{is} Surface tension at the solution-ice interface
τ Cloud optical depth
θ Potential temperature
ω Vertical wind component in isobaric coordinates

Subscripts
i Optical band number
k Microphysical bin number

[70] **Acknowledgments.** The authors wish to thank V. Khvorostyanov and H. Morrison for assisting with the implementation of the heterogeneous nucleation code. We also thank Z. Wang for supplying the radar-lidar cloud properties retrieval. Participation of Ruei-Fong Lin and David O'C. Starr in this study was supported by NASA's EOS Project Science Office and the Radiation Sciences Program. Research performed by Jennifer M. Comstock was supported by the DOE Office of Science, Atmospheric Radiation Measurement (ARM) Program.

References

Ackerman, T. P., and G. M. Stokes (2003), The Atmospheric Radiation Measurement program, *Phys. Today*, *56*, 38–44.

Ansmann, A., U. Wandinger, M. Riebesell, C. Weitkamp, and W. Michaelis (1992), Independent measurement of extinction and backscatter profiles in cirrus clouds by using a combined Raman elastic-backscatter lidar, *Appl. Opt.*, *31*, 7113–7131.

Baum, B. A., P. Yang, A. J. Heymsfield, S. Platnick, M. D. King, Y. X. Hu, and S. T. Bedka (2005), Bulk scattering properties for the remote sensing of ice crystals. part 2: Narrowband models, *J. Appl. Meteorol.*, *44*, 1896–1991.

Comstock, J. M., T. P. Ackerman, and D. D. Turner (2004), Evidence of high ice supersaturation in cirrus clouds using ARM Raman lidar measurements, *Geophys. Res. Lett.*, *31*, L11106, doi:10.1029/2004GL019705.

Comstock, J. M., et al. (2007), An intercomparison of microphysical retrieval algorithms for upper-tropospheric ice clouds, *Bull. Am. Meteorol. Soc.*, *88*, 191–204.

Corti, T., B. P. Luo, Q. Fu, H. Vomel, and T. Peter (2006), The impact of cirrus clouds on tropical troposphere-to-stratosphere transport, *Atmos. Chem. Phys.*, *6*, 2539–2547.

DeMott, P. J., D. C. Rogers, and S. M. Kreidenweis (1997), The susceptibility of ice formation in upper tropospheric clouds to insoluble aerosol components, *J. Geophys. Res.*, *102*, 19,575–19,584.

Ferrare, R. A., et al. (2004), Characterization of upper-troposphere water vapor measurements during AFWEX using LASE, *J. Atmos. Ocean. Technol.*, *21*, 1790–1808.

Field, P. R., R. Wood, P. R. A. Brown, P. H. Kaye, E. Hirst, R. Greenaway, and J. A. Smith (2003), Ice particle interarrival times measured with a fast FSSP, *J. Atmos. Ocean. Technol.*, *62*, 249–261.

Fu, Q. A. (1996), An accurate parameterization of the solar radiative properties of cirrus clouds for climate models, *J. Clim.*, *9*, 2058–2082.

Fu, Q., P. Yang, and W. B. Sun (1998), An accurate parameterization of the infrared radiative properties of cirrus clouds for climate models, *J. Clim.*, *25*, 2223–2237.

Gao, R. S., et al. (2004), Evidence that nitric acid increases relative humidity in low-temperature cirrus clouds, *Science*, *303*, 516–520.

Gayet, J.-F., et al. (2002), Quantitative measurement of the microphysical and optical properties of cirrus clouds with four different in situ probes: Evidence of small ice crystals, *Geophys. Res. Lett.*, *29*(24), 2230, doi:10.1029/2001GL014342.

Gettelman, A., and D. E. Kinnison (2007), The global impact of supersaturation in a coupled chemistry-climate model, *Atmos. Chem. Phys.*, *7*, 1629–1643.

Gettelman, A., E. J. Fetzer, A. Eldering, and F. W. Irion (2006), The global distribution of supersaturation in the upper troposphere from the Atmospheric Infrared Sounder, *J. Clim.*, *19*, 6089–6103.

Gierens, K. M., M. Monier, and J. F. Gayet (2003), The deposition coefficient and its role for cirrus clouds, *J. Geophys. Res.*, *108*(D2), 4069, doi:10.1029/2001JD001558.

Goff, J. A., and S. Gratch (1946), Low-pressure properties of water from −160 to 212 F, in *Transactions of the American Society of Heating and Ventilating Engineers*, pp. 95–122, 52nd Annual Meeting of the American Society of Heating and Ventilating Engineers, New York.

Goldsmith, J. E. M., F. H. Blair, S. E. Bisson, and D. D. Turner (1998), Turn-key Raman lidar for profiling atmospheric water vapor, clouds, and aerosols, *Appl. Opt.*, *37*, 4979–4990.

Gu, Y., and K. N. Liou (2000), Interactions of radiation, microphysics, and turbulence in the evolution of cirrus clouds, *J. Atmos. Sci.*, *57*, 2463–2479.

Gultepe, I., and D. O. Starr (1995), Dynamical structure and turbulence in cirrus clouds: Aircraft observations during FIRE, *J. Atmos. Sci.*, *52*, 4159–4182.

Haag, W., and B. Kärcher (2004), The impact of aerosols and gravity waves on cirrus clouds at midlatitudes, *J. Geophys. Res.*, *109*, D12202, doi:10.1029/2004JD004579.

Haag, W., B. Kärcher, J. Ström, A. Minikin, U. Lohmann, J. Ovarlez, and A. Stohl (2003), Freezing thresholds and cirrus cloud formation mechanisms inferred from in situ measurements of relative humidity, *Atmos. Chem. Phys.*, *3*, 1791–1806.

Hall, W. D., and H. R. Pruppacher (1976), The survival of ice particle falling from cirrus clouds in subsaturated air, *J. Atmos. Sci.*, *33*, 1995–2006.

Heymsfield, A. J., and J. Iaquinta (2000), Cirrus crystal terminal velocities, *J. Atmos. Sci.*, *57*, 916–938.

Heymsfield, A. J., and L. M. Miloshevich (1993), Homogeneous ice nucleation and supercooled liquid water in orographic wave clouds, *J. Atmos. Sci.*, *50*, 2335–2353.

Heymsfield, A. J., and L. M. Miloshevich (1995), Relative humidity and temperature influences on cirrus formation and evolution: Observations from wave clouds and FIRE II, *J. Atmos. Sci.*, *52*, 4302–4326.

Immler, F., K. Kruger, S. Tegtmeier, M. Fujiwara, P. Fortuin, G. Verver, and O. Schrems (2007), Cirrus clouds, humidity, and dehydration in the tropical tropopause layer observed at Paramaribo, Suriname (5.8°N, 55.2°W), *J. Geophys. Res.*, *112*, D03209, doi:10.1029/2006JD007440.

Jensen, E. J., and O. B. Toon (1997), The potential impact of soot particles from aircraft exhaust on cirrus clouds, *Geophys. Res. Lett.*, *24*, 249–252.

Jensen, E. J., O. B. Toon, D. L. Westphal, S. Kinne, and A. J. Heysmfield (1994), Microphysical modeling of cirrus. 1: Comparison with 1986 Fire IFO measurements, *J. Geophys. Res.*, *99*, 10,421–10,442.

Jensen, E. J., et al. (2001), Prevalence of ice-supersaturated regions in the upper troposphere: Implications for optically thin ice cloud formation, *J. Geophys. Res.*, *106*, 17,253–17,266.

Jensen, E., L. Pfister, T. Bui, A. Weinheimer, E. Weinstock, J. Smith, J. Pittman, D. Baumgardner, P. Lawson, and M. J. McGill (2005), Formation of a tropopause cirrus layer observed over Florida during CRYSTAL-FACE, *J. Geophys. Res.*, *110*, D03208, doi:10.1029/2004JD004671.

Kärcher, B., and U. Lohmann (2002), A parameterization of cirrus cloud formation: Homogeneous freezing of supercooled aerosols, *J. Geophys. Res.*, *107*(D2), 4010, doi:10.1029/2001JD000470.

Kärcher, B., and U. Lohmann (2003), A parameterization of cirrus cloud formation: Heterogeneous freezing, *J. Geophys. Res.*, *108*(D14), 4402, doi:10.1029/2002JD003220.

Kärcher, B., and J. Ström (2003), The roles of dynamical variability and aerosols in cirrus cloud formation, *Atmos. Chem. Phys.*, *3*, 823–838.

Kärcher, B., O. Möhler, P. J. DeMott, S. Pechtl, and F. Yu (2007), Insights into the role of soot aerosols in cirrus cloud formation, *Atmos. Chem. Phys.*, *7*, 4203–4227.

Kay, J. E., and R. Wood (2008), Timescale analysis of aerosol sensitivity during homogeneous freezing and implications for upper tropospheric water vapor budgets, *Geophys. Res. Lett.*, *35*, L10809, doi:10.1029/2007GL032628.

Khvorostyanov, V. I., and J. A. Curry (2000), A new theory of heterogeneous ice nucleation for application in cloud and climate models, *Geophys. Res. Lett.*, *27*, 4081–4084.

Khvorostyanov, V. I., and J. A. Curry (2004), The theory of ice nucleation by heterogeneous freezing of deliquescent mixed CCN. part I: Critical radius, energy, and nucleation rate, *J. Atmos. Sci.*, *61*, 2676–2691.

Khvorostyanov, V. I., and J. A. Curry (2005), The theory of ice nucleation by heterogeneous freezing of deliquescent mixed CCN. part II: Parcel model simulation, *J. Atmos. Sci.*, *62*, 261–285.

Khvorostyanov, V. I., J. A. Curry, J. O. Pinto, M. Shupe, B. A. Baker, and K. Sassen (2001), Modeling with explicit spectral water and ice microphysics of a two-layer cloud system of altostratus and cirrus observed during the FIRE Arctic Clouds Experiment, *J. Geophys. Res.*, *106*, 15,099–15,112.

Khvorostyanov, V. I., H. Morrison, J. A. Curry, D. Baumgardner, and P. Lawson (2006), High supersaturation and modes of ice nucleation in thin tropopause cirrus: Simulation of the 13 July 2002 Cirrus Regional Study of Tropical Anvils and Cirrus Layers case, *J. Geophys. Res.*, *111*, D02201, doi:10.1029/2004JD005235.

Koop, T., B. P. Luo, A. Tsias, and T. Peter (2000), Water activity as the determinant for homogeneous ice nucleation in aqueous solutions, *Nature*, *406*, 611–614.

Lawson, R. P., B. Baker, B. Pilson, and Q. Mo (2006), In situ observations of the microphysical properties of wave, cirrus, and anvil clouds. part II: Cirrus clouds, *J. Atmos. Sci.*, *63*, 3186–3203.

Lin, R. F., D. O. Starr, P. J. Demott, R. Cotton, K. Sassen, E. Jensen, B. Kärcher, and X. H. Liu (2002), Cirrus Parcel Model Comparison Project. Phase 1: The critical components to simulate cirrus initiation explicitly, *J. Atmos. Sci.*, *59*, 2305–2329.

Lin, R. F., D. O. Starr, J. Reichardt, and P. J. DeMott (2005), Nucleation in synoptically forced cirrostratus, *J. Geophys. Res.*, *110*, D08208, doi:10.1029/2004JD005362.

Liu, X. H., and J. E. Penner (2005), Ice nucleation parameterization for global models, *Meteorol. Z.*, *14*, 499–514.

Liu, X., J. E. Penner, S. J. Ghan, and M. Wang (2007), Inclusion of ice microphysics in the NCAR Community Atmospheric Model Version 3 (CAM3), *J. Clim.*, *20*, 4526–4547.

Lohmann, U., and B. Kärcher (2002), First interactive simulations of cirrus clouds formed by homogeneous freezing in the ECHAM general circulation model, *J. Geophys. Res.*, *107*(D10), 4105, doi:10.1029/2001JD000767.

Lohmann, U., B. Kärcher, and J. Hendricks (2004), Sensitivity studies of cirrus clouds formed by heterogeneous freezing in the ECHAM GCM, *J. Geophys. Res.*, *109*, D16204, doi:10.1029/2003JD004443.

Luo, B. P., Y. S. K. Kruger, G. G. Mace, and K.-M. Xu (2003), Cirrus cloud properties from a cloud-resolving model simulation compared to cloud radar observations, *J. Atmos. Sci.*, *60*, 510–525.

Mace, G. G., D. O. Starr, T. P. Ackerman, and P. Minnis (1995), Examination of coupling between an upper-tropospheric cloud system and synoptic-scale dynamics diagnosed from wind profiler and radiosonde data, *J. Atmos. Sci.*, *52*, 4094–4127.

Mace, G. G., T. P. Ackerman, E. E. Clothiaux, and B. A. Albrecht (1997), A study of composite citrus morphology using data from a 94-GHz radar and correlations with temperature and large-scale vertical motion, *J. Geophys. Res.*, *102*, 13,581–13,593.

Mace, G. G., T. P. Ackerman, P. Minnis, and D. F. Young (1998), Cirrus layer microphysical properties derived from surface-based millimeter radar and infrared interferometer data, *J. Geophys. Res.*, *103*, 23,207–23,216.

Mace, G. G., E. E. Clothiaux, and T. P. Ackerman (2001), The composite characteristics of cirrus clouds: Bulk properties revealed by one year of continuous cloud radar data, *J. Clim.*, *14*, 2185–2203.

Mace, G. G., A. J. Heymsfield, and M. R. Poellot (2002), On retrieving the microphysical properties of cirrus clouds using the moments of the millimeter-wavelength Doppler spectrum, *J. Geophys. Res.*, *107*(D24), 4815, doi:10.1029/2001JD001308.

Magee, N., A. M. Moyle, and D. Lamb (2006), Experimental determination of the deposition coefficient of small cirrus-like ice crystals near-50 degrees C, *Geophys. Res. Lett.*, *33*, L17813, doi:10.1029/2006GL026665.

Marcolli, C., S. Gedamke, T. Peter, and B. Zobrist (2007), Efficiency of immersion mode ice nucleation on surrogates of mineral dust, *Atmos. Chem. Phys.*, *7*, 5081–5091.

Matrosov, S. Y., and A. J. Heymsfield (2000), Use of Doppler radar to assess ice cloud particle fall velocity-size relations for remote sensing and climate studies, *J. Geophys. Res.*, *105*, 22,427–22,436.

McFarquhar, G. M., J. Um, M. Freer, D. Baumgardner, G. L. Kok, and G. Mace (2007), Importance of small ice crystals to cirrus properties: Observations from the Tropical Warm Pool International Cloud Experiment (TWP-ICE), *Geophys. Res. Lett.*, *34*, L13803, doi:10.1029/2007GL029865.

Meyers, M. P., P. J. DeMott, and W. R. Cotton (1992), New primary ice-nucleation parameterizations in an explicit cloud model, *J. Appl. Meteorol.*, *31*, 708–721.

Miloshevich, L. M., H. Vomel, A. Paukkunen, A. J. Heymsfield, and S. J. Oltmans (2001), Characterization and correction of relative humidity measurements from Vaisala RS80-A radiosondes at cold temperatures, *J. Atmos. Ocean. Technol.*, *18*, 135–156.

Mitchell, D. L. (1996), Use of mass- and area-dimensional power laws for determining precipitation particle terminal velocities, *J. Atmos. Sci.*, *53*, 1710–1723.

Moran, K. P., B. E. Martner, M. J. Post, R. A. Kropfli, D. C. Welsh, and K. B. Widener (1998), An unattended cloud-profiling radar for use in climate research, *Bull. Am. Meteorol. Soc.*, *79*, 443–455.

Murphy, D. M. (2003), Dehydration in cold clouds is enhanced by a transition from cubic to hexagonal ice, *Geophys. Res. Lett.*, *30*(23), 2230, doi:10.1029/2003GL018566.

Murray, B. J., D. A. Knopf, and A. K. Bertram (2005), The formation of cubic ice under conditions relevant to Earth's atmosphere, *Nature*, *434*, 202–205.

Nasiri, S. L., B. A. Baum, A. J. Heymsfield, P. Yang, M. R. Poellot, D. P. Kratz, and Y. Hu (2002), The development of midlatitude cirrus models for MODIS using FIRE-I, FIRE-II, and ARM in situ data, *J. Appl. Meteor.*, *41*, 197–217.

Orr, B. W., and R. A. Kropfli (1999), A method for estimating particle fall velocities from vertically pointing Doppler radar, *J. Atmos. Ocean. Technol.*, *16*, 29–37.

Pruppacher, H. (1995), A new look at homogeneous ice nucleation in supercooled water drops, *J. Atmos. Sci.*, *52*, 1924–1933.

Pruppacher, H. R., and J. D. Klett (1997), *Microphysics of Clouds and Precipitation*, 2nd ed., 954 pp., Springer, New York.

Quante, M., and D. O'C. Starr (2002), Dynamical processes in cirrus clouds: A review of observational results, in *Cirrus*, edited by D. K. Lynch et al., pp. 346–374, Oxford Univ. Press, New York.

Roeckner, E., R. Brokopf, M. Esch, M. Giorgetta, S. Hagemann, L. Kornblueh, E. Manzini, U. Schlese, and U. Schulzweida (2006), Sensitivity of simulated climate to horizontal and vertical resolution in the ECHAM5 atmosphere model, *J. Clim.*, *19*, 3771–3791.

Rogers, R., and M. K. Yau (1989), *A Short Course in Cloud Physics*, 3rd ed., 293 pp., Pergamon Press, Oxford, U. K.

Sassen, K., and S. Benson (2000), Ice nucleation in cirrus clouds: A model study of the homogeneous and heterogeneous modes, *Geophys. Res. Lett.*, *27*, 521–524.

Sassen, K., and J. M. Comstock (2001), A midlatitude cirrus cloud climatology from the facility for atmospheric remote sensing. part III: Radiative properties, *J. Atmos. Sci.*, *58*, 2113–2127.

Sassen, K., and G. C. Dodd (1988), Homogeneous nucleation rate for highly supercooled cirrus cloud droplets, *J. Atmos. Sci.*, *45*, 1357–1369.

Sassen, K., C. J. Grund, J. D. Spinhirne, M. M. Hardesty, and J. M. Alvarez (1990), The 27–28 October 1986 Fire IFO cirrus case-study—A 5 lidar overview of cloud structure and evolution, *Mon. Weather Rev.*, *118*, 2288–2311.

Sassen, K., L. Wang, D. O. Starr, J. M. Comstock, and M. Quante (2007), A midlatitude cirrus cloud climatology from the facility for atmospheric remote sensing. part V: Cloud structural properties, *J. Atmos. Sci.*, *64*, 2483–2501.

Shilling, J. E., M. A. Tolbert, O. B. Toon, E. J. Jensen, B. J. Murray, and A. K. Bertram (2006), Measurements of the vapor pressure of cubic ice and their implications for atmospheric ice clouds, *Geophys. Res. Lett.*, *33*, L17801, doi:10.1029/2006GL026671.

Spichtinger, P., and K. M. Gierens (2008), Modelling of cirrus clouds. part 2: Competition of different nucleation mechanisms, *Atmos. Chem. Phys. Discuss.*, *8*, 9061–9098.

Spichtinger, P., K. Gierens, H. G. J. Smit, J. Ovarlez, and J. F. Gayet (2004), On the distribution of relative humidity in cirrus clouds, *Atmos. Chem. Phys.*, *4*, 639–647.

Spichtinger, P. K., K. Gierens, and H. Wernli (2005), A case study on the formation and evolution of ice supersaturation in the vicinity of a warm conveyor belt's outflow region, *Atmos. Chem. Phys.*, *5*, 973–987.

Starr, D. O., and S. K. Cox (1985), Cirrus clouds. part II: Numerical experiments on the formation and maintenance of cirrus, *J. Atmos. Sci.*, *42*, 2682–2694.

Stephens, G. L. (1983), The influence of radiative transfer on the mass and heat budgets of ice crystals falling in the atmosphere, *J. Atmos. Sci.*, *40*, 1729–1739.

Stephens, G. L. (1984), The parameterization of radiation for numerical weather prediction and climate models, *Mon. Weather Rev.*, *112*, 826–867.

Tompkins, A. M. (2002), A prognostic parameterization for the subgrid-scale variability of water vapor and clouds in large-scale models and its use to diagnose cloud cover, *J. Atmos. Sci.*, *59*, 1917–1942.

Tompkins, A. M., K. Gierens, and G. Rädel (2007), Ice supersaturation in the ECMWF integrated forecast system, *Q. J. R. Meteorol. Soc.*, *133*, 53–63.

Toon, O. B., R. P. Turco, D. Westphal, R. Malone, and M. S. Liu (1988), A multidimensional model for aerosols—Description of computational analogs, *J. Atmos. Sci.*, *45*, 2123–2143.

Turner, D. D., and J. E. M. Goldsmith (1999), Twenty-four-hour Raman lidar water vapor measurements during the Atmospheric Radiation Measurement program's 1996 and 1997 water vapor intensive observation periods, *J. Atmos. Ocean. Technol.*, *16*, 1062–1076.

Turner, D. D., R. A. Ferrare, and L. A. Brasseur (2001), Average aerosol extinction and water vapor profiles over the southern great plains, *Geophys. Res. Lett.*, *28*, 4441–4444.

Wang, Z., and K. Sassen (2002a), Cirrus cloud microphysical property retrieval using lidar and radar measurements. part I: Algorithm description and comparison with in situ data, *J. Appl. Meteorol.*, *41*, 218–229.

Wang, Z., and K. Sassen (2002b), Cirrus cloud microphysical property retrieval using lidar and radar measurements. part II: Midlatitude cirrus microphysical and radiative properties, *J. Atmos. Sci.*, *59*, 2291–2302.

Whiteman, D. N., S. H. Melfi, and R. A. Ferrare (1992), Raman lidar system for the measurement of water-vapor and aerosols in the Earth's atmosphere, *Appl. Opt.*, *31*, 3068–3082.

Widener, K. B., and K. Johnson (2005), Millimeter wave cloud radar (MMCR) handbook, *Dept. of Energy, Atmos. Rad. Meas. Program Tech. Rep. ARM TR-018*, 22 pp. (Available at http://www.arm.gov)

Wood, S. E., M. B. Baker, and D. Calhoun (2001), New model for the vapor growth of hexagonal ice crystals in the atmosphere, *J. Geophys. Res.*, *106*, 4845–4870.

Wu, T., W. R. Cotton, and W. Y. Y. Cheng (2000), Radiative effects on the diffusional growth of ice particles in cirrus clouds, *J. Atmos. Sci.*, *57*, 2892–2904.

Xie, S., R. T. Cederwall, M. Zhang, and J. J. Yio (2003), Comparison of SCM and CSRM forcing data derived from the ECMWF model and from objective analysis at the ARM SGP site, *J. Geophys. Res.*, *108*(D16), 4499, doi:10.1029/2003JD003541.

Xie, S., R. T. Cederwall, and M. H. Zhang (2004), Developing long-term single-column model/cloud system-resolving model forcing data using numerical weather prediction products constrained by surface and top of the atmosphere observations, *J. Geophys. Res.*, *109*, D01104, doi:10.1029/2003JD004045.

Yang, P., K. N. Liou, K. Wyser, and D. Mitchell (2000), Parameterization of the scattering and absorption properties of individual ice crystals, *J. Geophys. Res.*, *105*, 4699–4718.

Yang, P., H. Wei, H.-L. Huang, B. A. Baum, Y. X. Hu, G. W. Kattawar, M. I. Mishchenko, and Q. Fu (2005), Scattering and absorption property database for nonspherical ice particles in the near- through far-infrared spectral region, *Appl. Opt.*, *44*, 5512–5523.

Zhang, M. H., and J. L. Lin (1997), Constrained variational analysis of sounding data based on column-integrated budgets of mass, heat, moisture, and momentum: Approach and application to ARM measurements, *J. Atmos. Sci.*, *54*, 1503–1524.

Zhang, M. H., J. L. Lin, R. T. Cederwall, J. J. Yio, and S. C. Xie (2001), Objective analysis of ARM IOP data: Method and sensitivity, *Mon. Weather Rev.*, *129*, 295–311.

J. M. Comstock, Atmospheric Science and Global Change Division, Pacific Northwest National Laboratory, P.O. Box 999, MSIN K9-24, Richland, WA 99352, USA. (jennifer.comstock@pnl.gov)

R.-F. Lin, Goddard Earth Sciences and Technology Center, University of Maryland, NASA Goddard Space Flight Center, Code 912, Mailstop 613.1, Greenbelt, MD 20771, USA.

D. O'C. Starr, Laboratory for Atmospheres, NASA Goddard Space Flight Center, Code 912, Greenbelt, MD 20771, USA.

P. Yang, Department of Atmospheric Sciences, Texas A&M University, 1204 Eller Building, 3150 TAMU, College Station, TX 77843-3150, USA.